

Cryo-EM structure of an activated GPCR-G protein complex in lipid nanodiscs

Meng Zhang ^{1,8}, Miao Gui ^{1,8}, Zi-Fu Wang¹, Christoph Gorgulla^{1,2,3}, James J. Yu¹, Hao Wu¹, Zhen-yu J. Sun¹, Christoph Klenk ^{1,2}, Lisa Merklinger⁴, Lena Morstein⁴, Franz Hagn ^{1,2,4}, Andreas Plückthun ^{1,2}, Alan Brown ^{1,2}, Mahmoud L. Nasr^{7,2} and Gerhard Wagner ^{1,2}

G-protein-coupled receptors (GPCRs) are the largest superfamily of transmembrane proteins and the targets of over 30% of currently marketed pharmaceuticals. Although several structures have been solved for GPCR-G protein complexes, few are in a lipid membrane environment. Here, we report cryo-EM structures of complexes of neurotensin, neurotensin receptor 1 and $G\alpha_n\beta_1\gamma_1$ in two conformational states, resolved to resolutions of 4.1 and 4.2 Å. The structures, determined in a lipid bilayer without any stabilizing antibodies or nanobodies, reveal an extended network of protein-protein interactions at the GPCR-G protein interface as compared to structures obtained in detergent micelles. The findings show that the lipid membrane modulates the structure and dynamics of complex formation and provide a molecular explanation for the stronger interaction between GPCRs and G proteins in lipid bilayers. We propose an allosteric mechanism for GDP release, providing new insights into the activation of G proteins for downstream signaling.

-protein-coupled receptors (GPCRs) sense extracellular stimuli such as odorants, hormones, neurotransmitters and photons 1,2 . A stimulus leads to a shift in the conformational equilibrium of the GPCR towards a state that favors binding of the intracellular signal transducer, guanosine diphosphate (GDP)-bound heterotrimeric G $\alpha\beta\gamma$ protein Binding causes perturbation of the GDP-binding pocket, leading to replacement of GDP by guanosine triphosphate (GTP) and dissociation of the G α and G $\beta\gamma$ subunits from each other and the GPCR The released G α and G $\beta\gamma$ subunits remain anchored to the membrane through lipid modifications but diffuse and interact with downstream effectors to stimulate signaling cascades 3 .

Recent advances in X-ray crystallography and cryo-EM have allowed the determination of several GPCR-G protein complex structures⁵⁻¹⁸. However, owing to difficulties in preparing stable GPCR-G protein complexes in detergent micelles, a range of stabilization techniques have had to be employed for most of the previously reported structures, including binding to antibodies or nanobodies, dominant-negative Gα subunits, or mini-G proteins that lack the α -helical domain (AHD) of $G\alpha$. Furthermore, the majority of previous structural studies reconstituted GPCR-G protein complexes in detergent micelles, with the only exception being a recently published structure of the D2 dopamine receptor (DRD2) in complex with a dominant-negative G_i and a stabilizing antibody scFv16 in lipid nanodiscs (NDs)19. The detergent structures fail to replicate the properties of the native lipid bilayer environment of GPCRs, including membrane thickness, lateral pressure and curvature²⁰. It has been reported that various GPCRs exhibit higher stability and better functionality when incorporated into lipid bilayers as compared to detergent micelles^{21,22}. Additionally, negatively charged

lipids have been found to allosterically modulate GPCR activation and its selective interaction with G proteins^{23–25}. Therefore, structural and dynamical information for the GPCR-G protein interaction in a lipid bilayer environment is necessary to understand the GPCR signal transduction mechanism.

To investigate the interaction between GPCR and G proteins in lipid bilayers, we used the neurotensin receptor 1 (NTSR1)-G_i interaction as a model system. NTSR1 is a class A GPCR that responds to neurotensin (NTS), a 13-residue peptide implicated in the pathogenesis of schizophrenia, antinociception, hypothermia, Parkinson's disease and tumor growth^{1,26}. To reconstitute and determine the structure of the NTS₈₋₁₃-NTSR1-G $\alpha_{i1}\beta_1\gamma_1$ complex in a lipid bilayer environment, we used circularized nanodiscs (cNDs) prepared with covalently circularized membrane scaffold proteins²⁷, which also allowed structure determination in the absence of external stabilizing factors. Comparison with structures of the GDP-bound G-protein heterotrimer²⁸ and GPCR-G protein complexes in detergent micelles, including the cryo-EM structure of the NTSR1- $G\alpha_{i1}\beta_1\gamma_2$ complex stabilized by scFv16 and in complex with a pseudopeptide analog of NTS¹², provide insights into the mechanism by which a G protein is activated by the interaction with GPCR in a lipid bilayer.

Results

Lipid bilayers promote efficient NTS-NTSR1-G $\alpha_{i1}\beta_1\gamma_1$ **complex formation.** To enable efficient expression of NTSR1 for purification and structural studies, we took advantage of the TM86V-L167R Δ IC3B construct²⁹. Compared to the inactive TM86V construct, TM86V-L167R contains a back mutation of L167R that restores NTSR1 functionality²⁹. The TM86V-L167R Δ IC3B²⁹ exhibits

¹Department of Biological Chemistry and Molecular Pharmacology, Blavatnik Institute, Harvard Medical School, Boston, MA, USA. ²Department of physics, Faculty of Arts and Sciences, Harvard University, Cambridge, MA, USA. ³Department of Cancer Biology, Dana-Farber Cancer Institute, Boston, MA, USA. ⁴Department of Biochemistry, University of Zurich, Zurich, Switzerland. ⁵Bavarian NMR Center at the Department of Chemistry, Technical University of Munich, Garching, Germany. ⁶Institute of Structural Biology, Helmholtz Center Munich, Neuherberg, Germany. ⁷Department of Medicine, Division of Renal Medicine, Division of Engineering in Medicine, Brigham and Women's Hospital, Harvard Medical School, Boston, MA, USA. ⁸These authors contributed equally: Meng Zhang, Miao Gui. ³E-mail: Alan_Brown@hms.harvard.edu; mnasr@bwh.harvard.edu; Gerhard_Wagner@hms.harvard.edu

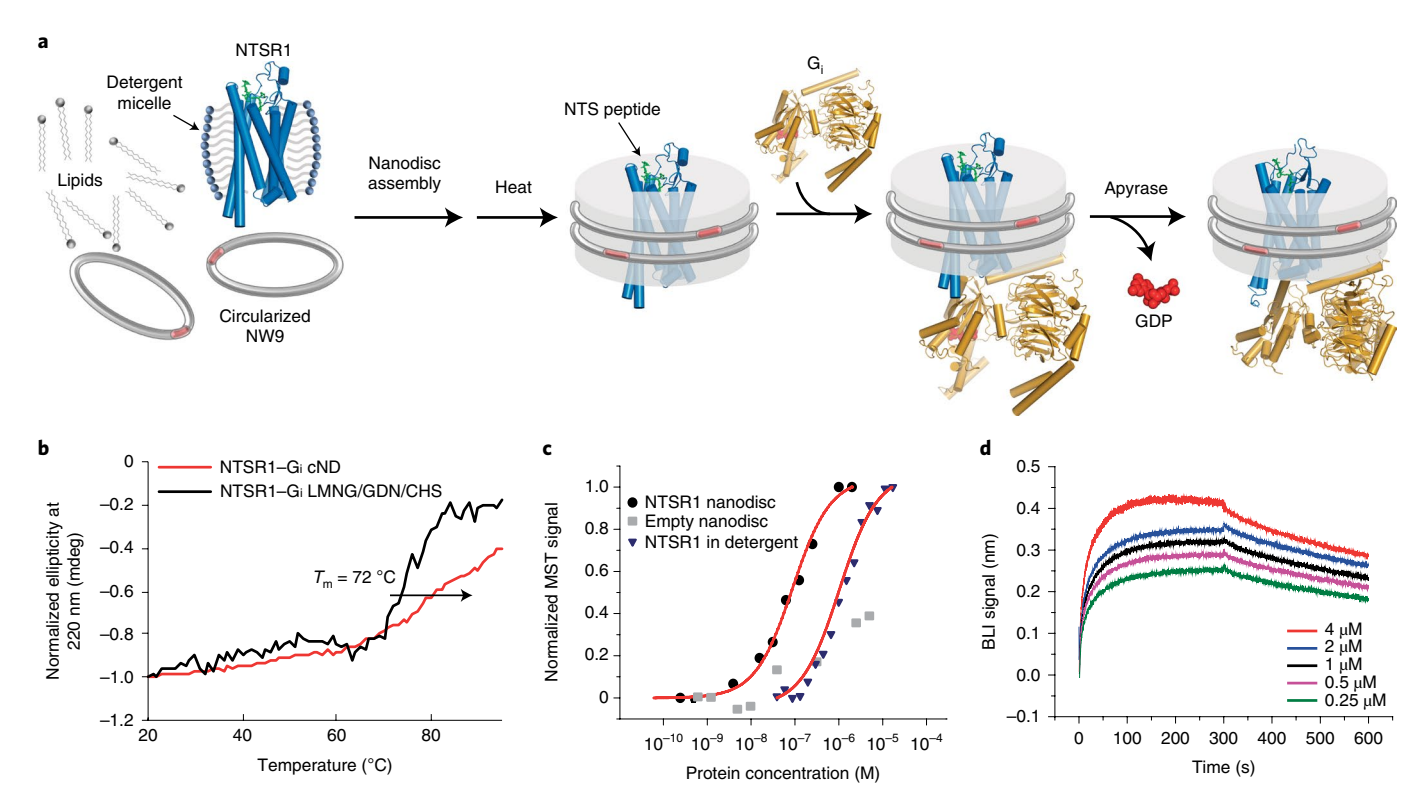


Fig. 1 Assembly and biophysical characterization of the NTS-NTSR1- G_n complex in cNDs. **a**, Schematic showing the assembly of the NTS-NTSR1- G_n complex in lipid NDs using the circularized membrane scaffold protein cNW9. **b**, CD thermostability assays on the NTS-NTSR1- G_n complex in LMNG/GDN/CHS micelles (black line) and in cNDs (red line). **c**, Microscale thermophoresis (MST) data fitting for the interaction between NTS-NTSR1 and G_n in diheptanoylphosphatidylcholine detergent (DH₂PC) yields a K_d of 1,400 ± 100 nM (blue triangles). The interaction between NTS-NTSR1-cND and G_n (black circles) yields a K_d of 76 ± 18 nM. Weak binding between empty NDs and G_n is shown as gray squares. A representative curve is shown for each sample. K_d values were calculated based on two independently prepared biological samples, each with three technical repeats. **d**, Bio-layer interferometry (BLI) traces of G_n binding to NTS-NTSR1-cND at five different concentrations. Data-fitting results are provided in Extended Data Fig. 2a,b. A representative curve is shown. K_d values were calculated based on three independently prepared biological samples.

downstream signaling functionality similar to that of wild-type NTSR1, as measured by the production of inositol-1-phosphate (IP1), the final metabolite of the inositol phosphate cascade, with a half-maximum effective concentration (EC50) of 2.7 nM for wild-type NTSR1 and 0.22 nM for TM86V-L167R Δ IC3B (Extended Data Fig. 1a, left). The single mutation of R167 $^{3.50}$ L (superscripts denote Ballesteros–Weinstein numbering 30) in the TM86V Δ IC3B construct completely quenched IP1 production (Extended Data Fig. 1a, right). As we discuss later, R167 $^{3.50}$ directly interacts with $G_{\rm i}$, partially explaining the critical role of this residue in the signaling process.

NTSR1 was affinity-purified using immobilized NTS₈₋₁₃, ensuring selection of properly folded NTSR1 only. The purified NTS-NTSR1 complex was then incorporated into 9-nm-diameter covalently circularized NDs containing a mixture of zwitterionic lipid 1-palmitoyl-2-oleoyl-sn-glycero-3-phosphocholine (POPC) and negatively charged lipid 1-palmitoyl-2-oleoyl-sn-glycero-3 -phosphoglycerol (POPG), and belted by circularized membrane scaffold protein cNW927 (Fig. 1a and Extended Data Fig. 1). Heat treatment of the purified NDs at 42°C for 24h improved sample homogeneity (Extended Data Fig. 1d). CD measurements showed increased thermostability of NTSR1 in cNDs compared to in detergent micelles, with a transition temperature (T_m) about 18 °C higher (Supplementary Fig. 1a-c). This sample was stable at 45°C for at least 15 days, showing well dispersed and reproducible peaks on two-dimensional (2D) NMR spectra (Supplementary Fig. 2a). These observations agree with studies showing that GPCRs are more stable in membrane environments³¹. When $G\alpha_{i1}\beta_1\gamma_1$ was incorporated into cNDs using the same method, its thermostability also improved relative to in detergent micelles (Supplementary Fig. 1d-f).

To reconstitute the signaling complex, we incubated NTS-NTSR1-cND with wild-type human $G\alpha_{i1}\beta_1\gamma_1$, which is myristoylated on $G\alpha_{i1}$ and prenylated on $G\gamma_1$ (Extended Data Fig. 1e). The NTS-NTSR1- $G\alpha_{i1}\beta_1\gamma_1$ complex in cNDs exhibits high thermostability (Fig. 1b and Supplementary Fig. 1g,h), and the binding affinity of NTSR1 to $G\alpha_{i1}\beta_1\gamma_1$ is higher in cNDs than in detergent micelles (K_d of 76 nM compared to 1.4 μ M; Fig. 1c), reflecting the essential role the membrane plays in efficient GPCR-G protein complex formation. Further binding kinetic measurements revealed two binding modes in cNDs with K_d values of 5.8 nM and 38 nM, respectively (Fig. 1d and Extended Data Fig. 2a,b). The complex in cND is capable of GDP/GTP exchange, as shown by a much higher dissociation rate following addition of GTP γ S (Extended Data Fig. 2c). However, for the following structural studies, we used apyrase to hydrolyze free GDP, which stabilizes the NTS-NTSR1- $G\alpha_{i1}\beta_1\gamma_1$ complex.

Cryo-electron microscopy structure of the NTS-NTSR1- $G\alpha_{11}\beta_1\gamma_1$ complex in cNDs. The higher affinity and improved thermostability of the NTS-NTSR1- $G\alpha_{11}\beta_1\gamma_1$ complex in lipid bilayers relative to in detergent micelles allowed us to collect cryo-EM data (Fig. 2, Table 1 and Extended Data Fig. 3) for the complexes without the need for further stabilization by antibodies/nanobodies or engineered G proteins. Two-dimensional (2D) class averages showed intact complexes within cNDs with uniform diameters of 9 nm (Extended Data Fig. 3). Three-dimensional classification of these projections revealed two well-resolved classes, corresponding to

	NTS-NTSR1-G _i -cND canonical state, AHD and ND mask out (EMD- 23099, PDB 7L0P)	NTS-NTSR1-G _i -cND canonical state, overall (EMD-23100, PDB 7L0Q)	NTS-NTSR1-G _i -cND noncanonical state, AHD and ND mask out (EMD-23101, PDB 7LOR)	NTS-NTSR1-G _i -cND noncanonical state, overall (EMD-23102, PDB 7LOS)
Data collection and processi	ng			
Magnification	105,000			
Voltage (kV)	300			
Electron exposure (e ⁻ /Å ²)	57			
Defocus range (μm)	−1.2 to −2.5			
Pixel size (Å)	0.825			
Symmetry imposed	C1			
Initial particle images (no.)	4,367,542			
Final particle images (no.)	575,791	575,791	324,002	324,002
Map resolution (Å)	4.1	4.3	4.2	4.5
FSC threshold	0.143	0.143	0.143	0.143
Refinement				
Refinement software	Coot 0.9-pre, Phenix-dev-3	318		
Initial model used (PDB code)	4BUO, 1GP2, 6OY9			
Map sharpening B factor ($Å^2$)	-245	-222	-204	-228
Model composition				
Nonhydrogen atoms	6,954	7,892	6,968	7,906
Protein residues	882 (6,896 atoms)	996 (7,834 atoms)	881 (6,910 atoms)	995 (7,848 atoms)
Ligands	1 (58 atoms)	1 (58 atoms)	1 (58 atoms)	1 (58 atoms)
B factors (Ų)				
Protein	73.6	69.75	73.63	69.79
Ligand	66.76	66.76	66.76	66.76
R.m.s. deviations				
Bond lengths (Å)	0.006	0.007	0.007	0.008
Bond angles (°)	1.051	1.286	1.368	1.508
Validation				
MolProbity score	1.9	1.84	1.96	2
Clashscore	8.36	7.82	9.79	9.27
Poor rotamers (%)	0.53	0.7	1.05	1.39
Ramachandran plot				
Favored (%)	93.1	93.69	93.44	93.99
Allowed (%)	6.9	6.31	6.56	6.01
Disallowed (%)	0	0	0	0

canonical' (C) and 'noncanonical' (NC) states of the NTS–NTSR1– $G\alpha_{i1}\beta_1\gamma_1$ complex, at resolutions of 4.3 and 4.5 Å, respectively (Extended Data Fig. 3). Two main conformational states were also seen in the recent cryo-EM study of the scFv16-stabilized NTSR1– $G\alpha_{i1}\beta_1\gamma_2$ complex in detergent micelles¹², but, as we describe below, these states differ from those that we observe (Fig. 2c). Additional density surrounds NTSR1, corresponding to the cNW9 membrane scaffold protein and the lipid bilayer it encloses. Masking out these densities improved the resolutions of the canonical and noncanonical states to 4.1 Å and 4.2 Å, respectively (Extended Data Fig. 3). In these maps, the pitches of the helices and the many side chains are resolved (Extended Data Fig. 4), allowing us to confidently place and remodel prior atomic models of NTS, NTSR1 and $G\alpha_{i1}\beta_1\gamma_1$ (refs. ^{28,29,32}). The density of NTS is well revolved in both confor-

mations (Extended Data Fig. 4) and adopts a similar structure and interactions to those observed in detergent micelles 12,33 . The N-terminal helices of G β and G γ both show weak densities, presumably due to flexibility.

Compared to most reported structures $^{9-18}$, the AHD of $G\alpha_{i1}$ is resolved in both states (Fig. 2a and Extended Data Fig. 5a,b). In the few structures that do report the position of the AHD 5,6,8 , the position may be affected by crystal contacts and/or the nanobodies/antibodies that were included for stabilization (Extended Data Fig. 5c–f). Our structures lack these constraints and therefore more closely reflect the native orientation and localization of the AHD in the nucleotide-free state. In comparison to the crystal structure of the GDP-bound G_i trimer the AHD has moved away from its close association with the Ras-like domain of $G\alpha$ to interact with

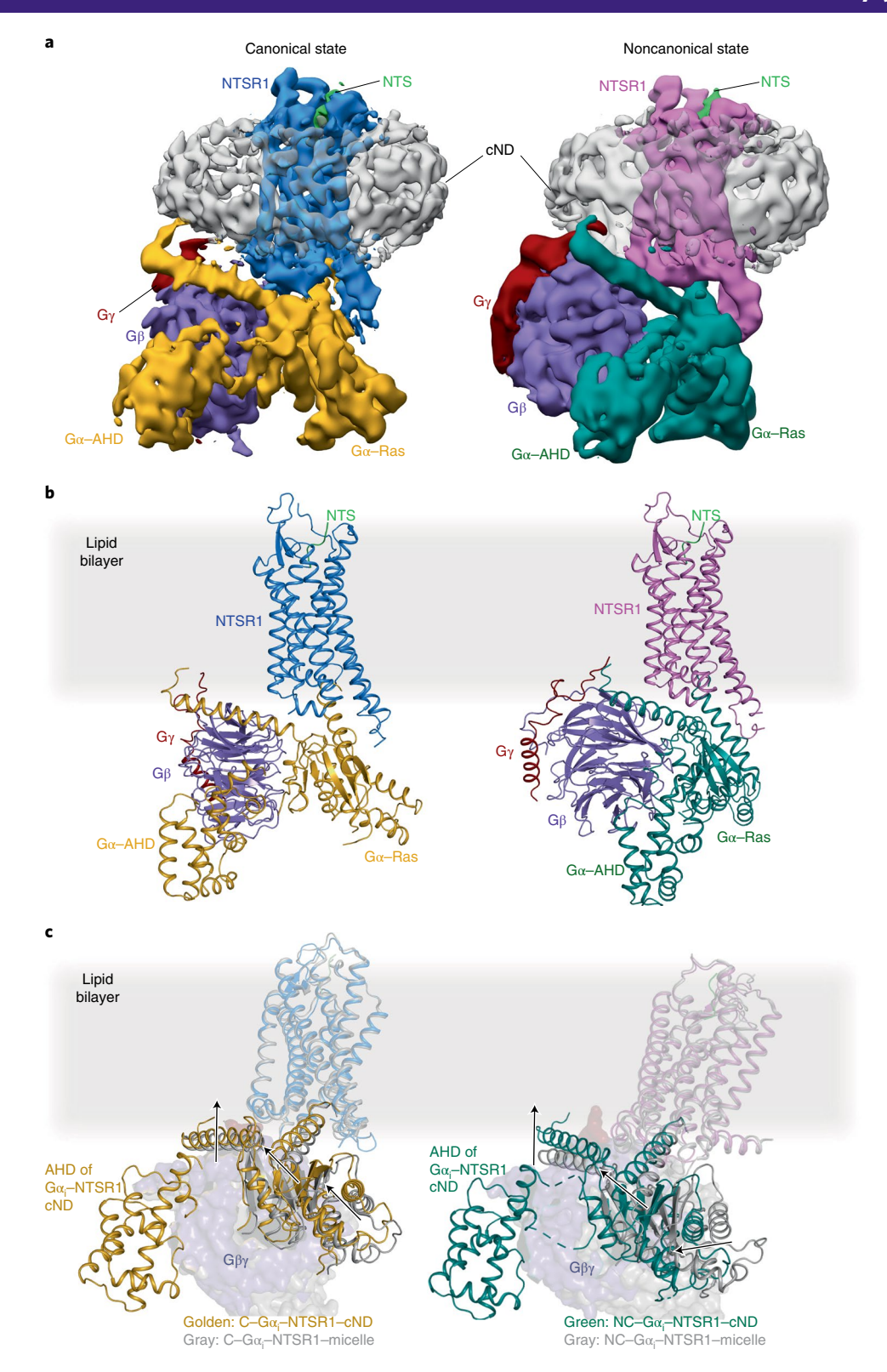


Fig. 2 | Cryo-EM structures of NTS-NTSR1-G_i-**cND. a**, Cryo-EM density maps of the NTS-NTSR1-G_i-cND complex in the canonical state (left) and noncanonical state (right). The maps are low-pass-filtered to 5 Å and colored by subunit. Higher-resolution maps were obtained by masking out density for the nanodisc (cND) and $G\alpha$ -AHD domain. **b**, Atomic models of the NTS-NTSR1-G_i-cND complex in the canonical state (left) and the noncanonical state (right). The models are shown in the same orientation as the maps in **a. c**, Structural superimposition of C-NTS-NTSR1-G_i-cND with C-NTSR1-G_i-scFv16-micelle (PDB 6OS9, left) and NC-NTS-NTSR1-G_i-cND with NC-NTSR1-G_i-scFv16-micelle (PDB 6OSA, right). Structural displacement is highlighted with arrows. The models are superimposed on the NTSR1.

the outer strands of the second and third β blades of G β (Fig. 2b and Extended Data Fig. 5a–c). As we discuss later, the large-scale movement of AHD is an important step in the GDP release pathway.

Lipid bilayer modulates the GPCR-G protein interaction. The NTS-NTSR1-G $\alpha_{i1}\beta_1\gamma_1$ complex shows interactions with the lipid bilayer in both the canonical and noncanonical states (Fig. 3a and

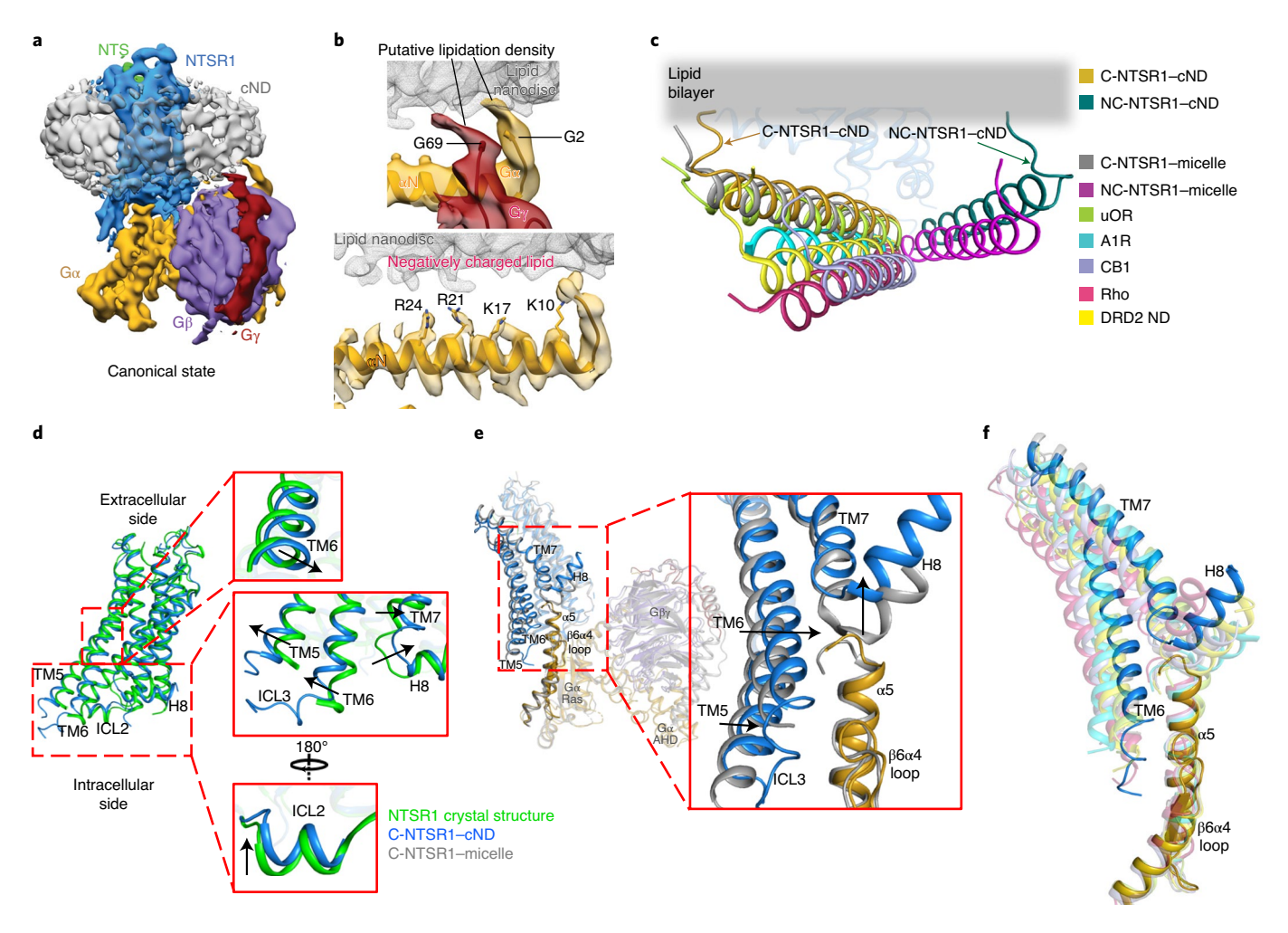


Fig. 3 | Impact of the lipid bilayer on the NTSR1-G_i **complex. a**, Cryo-EM density map of the NTS-NTSR1-G_i-cND complex in the canonical state, low-pass-filtered to 5 Å to aid visualization, and colored by subunit. **b**, Top: density for the putative lipid modifications of G2 of $G\alpha_{i1}$ and G69 of $G\gamma_1$. ND density is shown as a gray mesh. The density map of the canonical state is low-pass-filtered to 5 Å. Bottom: positively charged residues of the α N-helix of $G\alpha_{i1}$ face the negatively charged lipid bilayer. The 4.1 Å density map of the canonical state is shown. **c**, Comparison of the α N-helices of the GPCR-G_i complexes. C- and NC-NTSR1-cND indicate the canonical and noncanonical states of the NTS-NTSR1-G_i complex in NDs. C- and NC-NTSR1-micelle indicate the canonical and noncanonical states of the JMV449-NTSR1-G_i complex in detergent micelles. Other class A GPCR-G_i complexes shown are α (PDB 6DDE), A_iR-G_i (PDB 6D9H), CB1-G_i (PDB 6N4B), Rho-G_i (PDB 6CMO) and DRD2-G_i (PDB 6VMS). The models are superposed on the GPCR. **d**, Structural comparison between NTSR1 from the canonical-state NTS-NTSR1-G_i complex in lipid NDs (blue) and the crystal structure of NTSR1 in detergent (green). **e**, Structural comparison between the canonical states of NTSR1-G_i in lipid bilayer (blue) and detergent (gray), superposed on the Ras-like domain of Gα (gold). Zoomed view of the cytoplasmic side of TM5-TM6, ICL3 and TM7-H8, as well as the α5-helix and α4β6 loop of Gα. **f**, Comparison of the location of TM6 relative to the α5-helix of Gα in the C-state NTSR1 (blue) in complex with G_i (gold) with other class A GPCR-G_i complex structures (PDB IDs are as in **c**; colored as in **c**). The models are superposed on the Ras-like domain of Gα.

Extended Data Fig. 6). Density at the beginning of the αN-helix of $G\alpha$ is observed protruding into the lipid bilayer, which corresponds to the myristoylation site of the $G\alpha$ (Fig. 3b, top). Similar density at the C terminus of Gy corresponds to the prenylation site (Fig. 3b, top). Similar interactions are also observed in the DRD2-G_i structure¹⁹, the only other available GPCR-G_i complex structure in ND, revealing how protein lipidation helps anchor G proteins to membranes. Lipid density is also observed above the positively charged αN -helix of $G\alpha$ (Fig. 3b, bottom). The side chains of the arginine and lysine residues within this helix are oriented towards the membrane and probably form electrostatic interactions with the negatively charged lipid POPG (Fig. 3b, bottom). Consistent with previous observations that negatively charged lipids strengthen the interaction between NTSR1 and G protein²⁵, binding studies on the complex in a neutral lipid bilayer (POPC) resulted in weaker binding $(K_d \text{ of } 236 \text{ nM})$ than in negatively charged POPG (53 nM; Extended

Data Fig. 2f). Electrostatic interactions with the lipid headgroups may explain why the αN -helices of the complexes solved here are located closer to the membrane than in structures of class A GPCR- G_i complexes in detergent micelles (Fig. 3c). The αN -helix is also closer to the membrane than in the DRD2- G_i ND structure (Fig. 3c), perhaps reflecting differences among GPCR-G protein pairs or a consequence of the stabilizing single-chain antibody used in that structure. The observed hydrophobic and electrostatic interactions ensure close proximity of G_i to NTSR1, and thus enhance G_i binding to NTSR1, particularly between the αN - $\beta 1$ hinge of G_i and intracellular loop 2 (ICL2) of NTSR1 (Fig. 4).

As expected, the majority of NTSR1 is buried inside the lipid bilayer, including transmembrane helices (TM) 1–4 and TM7, the N-terminal half of TM5 and the C-terminal half of TM6. ICL2 and H8 are partially buried at the membrane surface (Extended Data Fig. 6c). Membrane burial of H8 is also observed in the DRD2–G_i

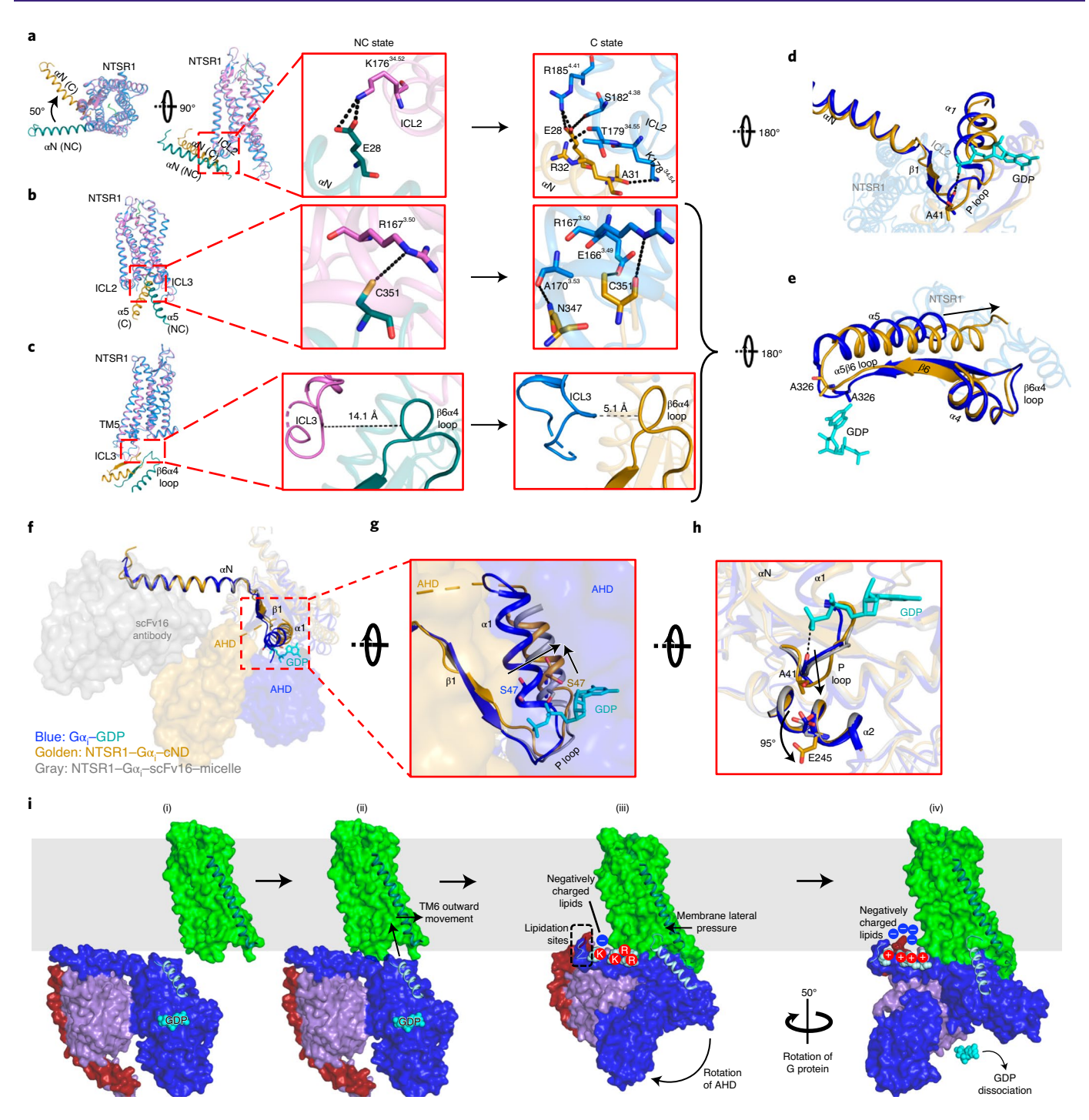


Fig. 4 | Allosteric modulation of the GDP-binding pocket by the NTSR1-G_i interaction. a-c, Superposition between canonical-state NTSR1 (blue) and the αN-helix of Gα (gold) with the noncanonical-state NTSR1 (orchid) and αN-helix of Gα (dark cyan). Models are superposed on NTSR1. Overview (left) and zoomed views of the noncanonical state (middle) and canonical state (right) for ICL2-αN-helix interactions (**a**) (compared to the noncanonical state, the αN-helix of Gα of the canonical state is rotated by 50°); NTSR1-α5-helix interactions (**b**); ICL3-α4β6 loop interactions (**c**). The backbones of ICL3 and α4β6 are closer in the canonical state and form interactions predicted by molecular dynamics simulations (Extended Data Fig. 10a). **d,e**, Intracellular views showing perturbation of the P loop (**d**) and β6α5 loop (**e**) in the canonical state (gold) relative to the crystal structure of GDP-bound G_i (blue; GDP in cyan, PDB 1GP2). Models are superposed on the Gα Ras-like domain. **f**, Structures of GDP-bound Gα_i (blue; GDP in cyan, PDB 1GP2), NTSR1-bound Gα_i in detergent (gray, PDB 6OS9) and NTSR1-bound Gα_i in a lipid bilayer (gold) showing the different locations of the AHD and the stabilizing antibody scFv16. The structures are superposed on αN-β1. **g**, Zoomed view showing lateral displacement of the α1-helix, including S47 from the phosphates of GDP in NTSR1-G_i-cND. **h**, Rotation of the side chain of E245 in NTS-NTSR1-G_i-cND (gold) by 95° compared to the GDP-G_i structure (blue, PDB 1GP2) to sterically accommodate the P loop. This rotation is not observed in detergent (gray, PDB 6OS9). **i**, Model of the proposed insertion-rotation mechanism: (i) lateral diffusion of NTSR1 and G_i; (ii) recognition of NTSR1 by G_i, allowing insertion of α5 into the open cavity of NTSR1; (iii) formation of the noncanonical state including displacement of the AHD; (iv) formation of the canonical state following rotation of G_i.

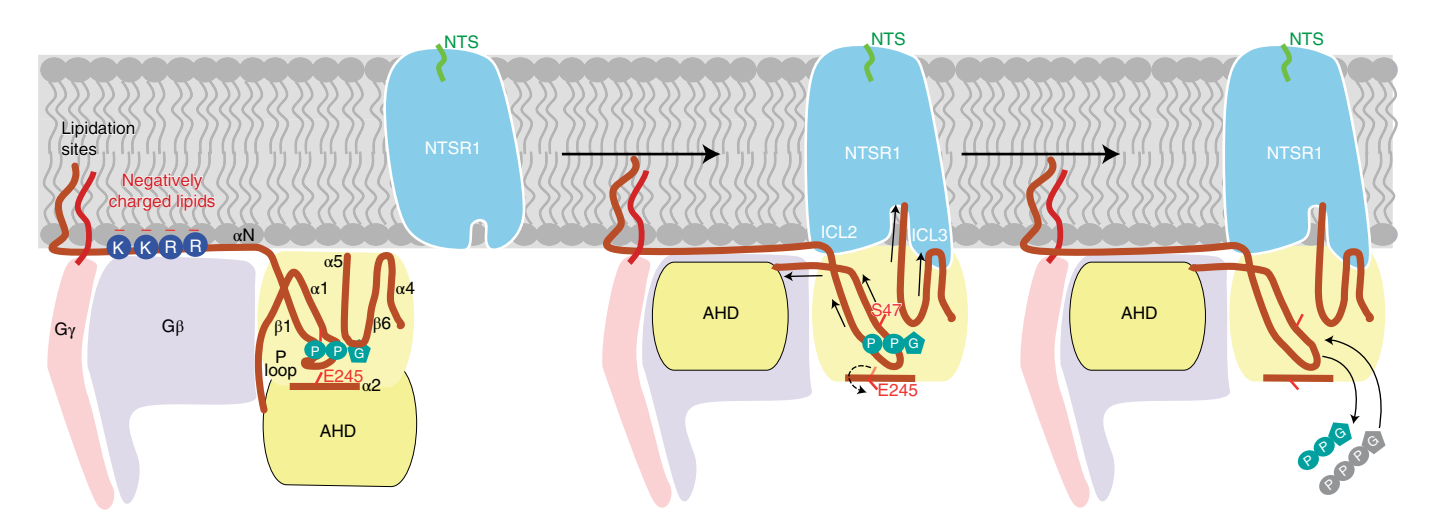


Fig. 5 | Proposed mechanism of GDP release. The interaction between G_i and NTSR1 leads to allosteric modulation of the GDP-binding site via three pathways. (1) Movement of the AHD to G_i is correlated with movement of the directly linked G_i . Movement of G_i results in its dissociation from the phosphate groups of GDP. (2) Interaction between ICL2 of NTSR1 and the G_i Phinge of G_i perturbs the P loop though G_i resulting in dissociation of the P-loop from the phosphate groups of GDP, which is coupled with a 95° rotation of the side chain of E245 on G_i . (3) Interactions between G_i and the core of NTSR1 and between the G_i Phinge of G_i Phinge of GDP. The transition of G_i increases G_i flexibility, resulting in dissociation of G_i from AHD and GDP. The multi-point coordination of these structural elements leads to dissociation of GDP from G_i . Release of GDP vacates the nucleotide-binding pocket for subsequent GTP binding, thus completing the GDP/GTP exchange process.

ND structure¹⁹. To reveal the effects of the lipid bilayer on the GPCR, we compared our structures with the crystal structure of rat NTSR1 (X-rNTSR1, PDB 4XEE)33 and the cryo-EM structure of human NTSR1 in the canonical state (C-hNTSR1, PDB 6OS9)12 (representing structures of agonist-bound NTSR1 in detergent in the absence and presence of G_i, respectively). In lipid bilayers, the core of NTSR1 is more compact due to an inward movement of the middle of TM6 (Fig. 3d and Extended Data Fig. 7a), whereas X-rNTSR1 and C-hNTSR1 superpose well with each other (Extended Data Fig. 7b). Compression of TM6 is probably due to lateral pressure from the lipid bilayer. It is also possible, in principle, that the compression is caused by stabilization mutations in our construct (Extended Data Fig. 1b), but examination of structures of NTSR1 with very different mutations (PDB 4BUO, 3ZEV and 4BWB) shows that these structures are virtually identical²⁹. Additionally, only one of these mutations is in TM6 (H^{6.32}R). This conservative mutation maintains hydrogen bonding with V7.56, suggesting that it has little impact on the overall position of TM6. Relative to the detergent structures, ICL2 and the cytoplasmic side of TM7 and H8 show an upward movement, indicative of membrane association (Fig. 3d and Extended Data Fig. 7a). Overall, the increased compaction and better membrane association of NTSR1 agrees with the improved thermostability observed in lipid bilayers (Fig. 1b and Supplementary Fig. 1g,h).

Following insertion of the α 5-helix of $G\alpha$ into the core of NTSR1, the cytoplasmic side of TM5, TM6 and ICL3 move outward to accommodate the α 5-helix (Fig. 3d). Structural and dynamical changes are also observed in 2D NMR experiments on $^1H^{15}N$ -NTSR1 upon binding to G_i in cNDs (Supplementary Fig. 2c). In the presence of the lipid bilayer, this movement appears to be more restricted than the large outward movement observed in detergent, potentially due to the lateral pressure from the lipid bilayer (Fig. 3e). The reduced movement of TM5 and TM6 relative to C-hNTSR1 maintains closer contacts with the α 5-helix (Fig. 3e). Comparison of TM6 positions among class A GPCR– G_i complexes shows that TM6 in the canonical-state NTSR1 exhibits closest proximity to the α 5-helix, resulting in more potential interactions (Fig. 3f and Extended Data Fig. 7c). Taken together, these observations suggest that the lipid bilayer constrains the conformation of NTSR1 to

enhance its interaction with G_i, agreeing with our observation of higher binding affinity in lipid bilayer (Fig. 1c).

The NTSR1- $G\alpha_{ij}\beta_{j}\gamma_{j}$ interface. The canonical and noncanonical states show different NTSR1-G, interactions, with a total buried surface area of 1,285 Å² in the canonical state and 1,185 Å² in the noncanonical state. The two states are related by a 50° rotation of G_i relative to NTSR1 (Fig. 4a). This change in orientation results in different interactions between the αN-helix and ICL2. In the canonical state, a potential salt bridge is observed between E28 and R1854.41, as well as potential hydrogen bonds between E28 and S1824.38, R32 and T17934.55, and A31 and K17834.54 (Fig. 4a). By contrast, only one potential hydrogen bond (between R32 and T17834.55) is observed in C-hNTSR1 in detergent micelles¹². These additional contacts with ICL2 in the presence of the lipid bilayer probably result from the closer proximity of the αN-helix to the membrane and NTSR1 (Fig. 3c). In addition, the highly conserved bulky residue F17534.51 in ICL2 is inserted into a hydrophobic pocket within Gα, involving residues F336 and V339 on α5 as well as L194 on β3 (Extended Data Fig. 8b). This interaction has been suggested to be important for GDP dissociation for secondary GPCR-G_{i/o} coupling, such as NTSR1-G_i (ref. ³⁴). Many of these interactions are absent in the noncanonical state, where we observe only one potential salt bridge between E28 and K176^{34.52}. Fewer contacts in the noncanonical state suggest that it could be less stable than the canonical-state complex. These interactions are not observed in the NTSR1-β-arrestin1 complex structure³⁵, implying an important role for ICL2 in transducer selectivity for downstream signaling.

The orientation of the $\alpha 5$ -helix relative to NTSR1 is also different between the two states, although the depth of insertion is the same (Fig. 4b). Examination of multiple class A GPCR– G_i structures shows that it is common for the $\alpha 5$ insertion to stop at $R^{3.50}$ (Extended Data Fig. 9d). Thus, $R^{3.50}$ might serve as both an interaction hotspot and a 'stopping point' that decides the depth of the $\alpha 5$ insertion. In the canonical state, several potential hydrogen bonds are observed between $\alpha 5$ and NTSR1, including C351 with E166 $^{3.49}$, C351 with R167 $^{3.50}$, and N347 with A170 $^{3.53}$ (Fig. 4b). The interaction between N347 and A170 $^{3.53}$ is also observed in the C-hNTSR1 structure 12 . E166 $^{3.49}$ and R167 $^{3.50}$ belong to the highly conserved D/ERY motif.

R167^{3.50} is found to be essential for downstream signaling (Extended Data Fig. 1a) and has been reported to be critical for GDP/GTP exchange through mutagenesis studies²⁹. The noncanonical state displays fewer interactions with only one possible hydrogen bond between C351 and R167^{3.50} (Fig. 4b).

Rotation of G_i also results in the $\alpha 4\beta 6$ loop moving closer to ICL3 in the canonical state than in either the noncanonical state (Fig. 4c) or detergent structures (Extended Data Fig. 9b). Although the map quality of ICL3 prevents a detailed analysis, molecular dynamics simulations show potential salt bridges and hydrogen bonds forming between ICL3 and the $\alpha 4\beta 6$ loop in the canonical state (Extended Data Fig. 10). Similar interactions between ICL3 and the $\alpha 4\beta 6$ loop have been observed in the structure of the adenosine A1 receptor (A_1R)– $G\alpha_{12}\beta_1\gamma_2$ complex¹⁶.

Compared to detergent NTSR1– G_i structures, the cND structures in the current study have several additional interactions between G_i and NTSR1, namely between E28 and R185^{4,41}, E28 and S182^{4,38}, A31 and K178^{34,54}, E28 and K176^{34,52}, and C351 with E166^{3,49}. To verify the importance of these interactions, we mutated R185^{4,41}, S182^{4,38}, K178^{34,54}, K176^{34,52} and E166^{3,49} to alanine and measured binding affinity in cNDs using microscale thermophoresis (MST). The 5-alanine mutant shows weaker binding than the unmutated construct (K_d of 347 nM compared to 76 nM) (Extended Data Fig. 2e), suggesting that the additional interactions observed in the cND complex structure contribute to the higher binding affinity compared to the detergent structure.

Structural changes in the GDP-binding pocket of G_i. Comparison between the NTSR1-bound G_i and GDP-bound G_i (PDB 1GP2) shows structural changes in the GDP-binding pocket. This pocket consists of two loops: the $\beta6\alpha5$ loop that binds the guanine ring of GDP and the $\beta 1\alpha 1$ loop (the P loop) that binds the phosphates of GDP. In the presence of NTSR1, both loops adopt different conformations. The β6α5 loop moves away from GDP, showing dissociation between A326 and the guanine ring (Fig. 4d). The P loop that wraps around GDP in the GDP-bound G_i structure and the detergent NTR1-bound G_i structure unwraps GDP in the lipid bilayer, showing dissociation between A41 and the β-phosphate of GDP. The displacement of the P loop appears sterically coordinated with a 95° rotation of the side chain of E245 α2 (Fig. 4h). In addition, movement of all appears to be correlated with movement of the AHD to which it is tethered. The AHD-linked α1 moves both horizontally and vertically away from GDP, potentially displacing S47 from the phosphate of GDP (Fig. 4f,g). Similar changes are not observed in the detergent NTSR1-G_i complex structures (Fig. 4f-h). These observations, when combined with previously reported findings, allow us to propose a more complete mechanism for GDP release, as discussed in the following.

Discussion

An insertion-rotation model for G_i activation. Comparison of our two conformational states with one another and with previous structures allows us to propose a mechanism of G-protein activation in a lipid environment. The presence of more GPCR-G_i contacts in the canonical state than the noncanonical state suggests that the noncanonical state might be an intermediate, lower-affinity state. This implies that, in addition to the close proximity between GPCR and G_i regulated by the lipid bilayer, a certain orientation of G_i relative to GPCR is also required to enable efficient complex formation. This is consistent with our kinetics experiments, which showed both high-affinity (5.8 nM) and lower-affinity (38 nM) binding modes (Fig. 1d and Extended Data Fig. 2). A sequential model was also proposed to link the states observed with scFv16-stabilized hNTSR1-G_i in detergent micelles¹². Following this hypothesis, it appears that the interaction between NTSR1 and G_i goes through an insertion-rotation mechanism (Fig. 4i). NTSR1

and G_i first laterally diffuse in the membrane until they meet. The cavity in NTSR1 allows insertion of the α 5-helix into the open core of NTSR1. Subsequently, G_i rotates around α 5 by \sim 50°, which maximizes protein–protein interactions (Fig. 4 and Extended Data Fig. 9). The rotation stops when the α 4 β 6 loop collides with ICL3, the α N- β 1 hinge is caught by ICL2, the F336 hydrophobic pocket encircles F175³^{4,51}, and the α 5-helix forms most contacts with the core of NTSR1, eventually leading to GDP dissociation. Alternately, full insertion of the α 5-helix in both states (Extended Data Fig. 9d) may happen after GDP dissociation, as it has been reported that changes in α 5 conformation continue long after GDP release⁴. This flexible interaction between α 5 and the core of NTSR1 might facilitate subsequent GTP association and downstream signaling.

A multipartite mechanism for GPCR-catalyzed nucleotide exchange. Based on a comparison of our structures with the structure of GDP-G_i (ref. ²⁸), we propose a multipartite mechanism for receptor-catalyzed nucleotide exchange (Fig. 5) that is supported by previous functional studies. In the unbound G-protein, the nucleotide is buried between the Ras-homology domain (RHD) and the AHD of Ga. It has been suggested that when the G protein encounters the receptor, the α5-helix is straightened and forms early interactions with the GPCR, which initiates the GDP release process³⁶. The AHD dissociates from the RHD and, as we show here, interacts with the outermost strands of GB (Extended Data Fig. 5a,b). Similar observations have also been reported for the rhodopsin-G_T complex structure, which shows stabilization of AHD by Gβ³². Previous computational simulations have shown that separation of the AHD is necessary (presumably to create an exit pathway for GDP) but not sufficient for rapid nucleotide release^{37,38}. Here, we observe that multiple allosteric pathways converge on structural rearrangements of the GDP-binding site, and it is the combination of these pathways that is responsible for GDP dissociation.

In the first pathway, insertion and rotation of the α 5-helix into the core of NTSR1 by two helical turns compared to the GDP-G_i structure²⁸ displaces the $\beta6\alpha5$ loop, which is responsible for binding the guanine ring of GDP in the nucleotide-bound state (Fig. 4e). This is consistent with structural studies showing that perturbation of the $\beta6\alpha5$ loop induced by the rotational translation of the α5-helix is essential for GDP dissociation^{5,6,8–18,32,39,40}. As a result of this perturbation, A326 in the highly conserved TCAT motif moves away from its position in the GDP-G_i structure, resulting in loss of contact with GDP. This agrees with a previous mutagenesis study showing that A326 is essential for GDP binding⁴¹. The conformation of the α 5 β 6 loop is different from that in the detergent structure, potentially as a result of the different angles with which the α 5-helix inserts into NTSR1 (Extended Data Fig. 9c,d). This agrees with computational simulations in which the tilt angle of the α 5-helix was found to directly correlate with the conformation of the $\beta6\alpha5$ loop³⁸. The new conformation of the $\beta6\alpha5$ loop, and therefore the dynamics of GDP loss, may be affected by the neighboring interaction between ICL3 and the α4β6 loop (Fig. 4c,e and Extended Data Fig. 10). Insertion of α5 also breaks the highly conserved hydrophobic pocket linking F336 on α 5 with α 1, β 2 and β 3 in the GDP-bound state (Extended Data Fig. 8a), while establishing a new hydrophobic network engaging the conserved bulky hydrophobic residue F17534.51 on ICL2 of NTSR1 (Extended Data Fig. 8b). As reported previously, this structural transition could increase the flexibility of α 1, which destabilizes its interaction with both the GDP and AHD, contributing to domain opening and GDP dissociation^{4,42,43}.

In the second pathway, displacement of AHD is probably coordinated with movement of the α 1-helix to which it is tethered (Fig. 4f,g). This lateral movement causes residues within α 1, including S47, to dissociate from the phosphate group of GDP (Fig. 4f,g). The S47N mutation is dominant-negative¹⁰, suggesting that this

movement is a key step towards GDP release. Furthermore, previous mutagenesis⁴⁴, hydrogen-deuterium exchange mass spectrometry $(HDX)^{39}$ and computational⁴⁵ studies have all suggested that perturbations in $\alpha 1$ play important roles in accelerating GDP dissociation.

In the third pathway, the interaction between ICL2 of NTSR1 and the αN-β1 hinge, including a potential salt bridge between E28 and R1854.41, and several potential hydrogen bonds between E28 and S182^{4.38}, R32 and T179^{34.55}, and A31 and K178^{34.54} (Fig. 4a), propagates through the β1 strand and perturbs the GDP-phosphate-binding P loop ($\beta 1\alpha 1$ loop) (Fig. 4d). P-loop perturbation by the $\alpha N\beta 1$ -ICL2 interaction is also supported by previous structural^{6,14,15} and HDX³⁹ studies. This perturbation results in a displacement of the P loop, breaking the interaction between the main chain of residue A41 and the β-phosphate of GDP (Fig. 4d). To sterically accommodate the displaced P loop, the side chain of E245 on α2 has rotated by 95° (Fig. 4h). This implies a coupling of P-loop disorder with E245 rotation in the GDP dissociation process and, conversely, a role for E245 in maintaining a stable GDP-bound G-protein conformation, which coincides with the E245A mutant having a dominant-negative effect^{16,41}. This rotation is not observed in the detergent-embedded NTSR1-G structure, and the P loop adopts a conformation more similar to the one observed in the GDP-G_i structure²⁸ (Fig. 4h). In contrast to the NTSR1-G_i complex structures, the P loop of the recently reported β1AR-Gs complex structure is more disordered, which also leads to GDP dissociation. The different patterns of P-loop perturbation upon GPCR-G protein interaction could be due to different types of G protein.

Together, this multi-point coordination mechanism leads to dissociation of GDP from G_i and the creation of a free nucleotide-binding pocket for GTP association (Fig. 5).

Understanding the structural basis for the interaction between GPCRs and G proteins under physiological conditions has been challenging due to the poor stability of the complexes in detergent micelles. Most of the published structures required antibodies/ nanobodies and/or engineered G proteins for additional stability, which rendered the complexes incapable of GDP/GTP exchange. Using our recently developed covalently circularized NDs²⁷, we have determined two structures, representing different conformational states, of the NTS-NTSR1- $G\alpha_{i1}\beta_1\gamma_1$ complex in a lipid bilayer, without the need for external stabilization. These structures identified several additional interaction hotspots between NTSR1 and G_i as compared to the detergent structures, explaining the observation of a tighter binding and more stable NTSR1-G, complex in a lipid bilayer as compared to in detergent micelles. The lateral movement of TM6, which is considered a signature of active receptors in detergents, is found to be restricted by the membrane, highlighting the importance of the membrane in modulating the dynamics and binding affinities of GPCR-G protein interactions. Additionally, a combination of hydrophobic and electrostatic interactions between the lipid bilayer and G_i is uncovered, suggesting the importance of the membrane-G_i interaction in NTSR1-G_i complex formation. The absence of stabilizing antibody/nanobody enabled observation of unconstrained AHD movement, which contributes to a more complete view of the GDP dissociation mechanism. Our structures also revealed several conformational changes in the GDP-binding pocket that are absent in the detergent structures, allowing us to unravel the interconnected roles of the NTSR1-G_i interaction, membrane-protein interaction and G-protein activation in the GDP dissociation process. The proposed multipartite allosteric mechanism of GDP release reveals a competition between GDP and NTSR1 for binding G_i. This observation agrees with a previous NMR study showing that the interaction between NTSR1 and $G\alpha$ is strongest when $G\alpha$ is nucleotide-free⁴⁶. Our study therefore provides new insights into the signal transduction process triggered by GPCR-G protein complex formation and will serve as a model for future studies of GPCR signaling in lipid bilayers.

Online content

Any methods, additional references, Nature Research reporting summaries, source data, extended data, supplementary information, acknowledgements, peer review information; details of author contributions and competing interests; and statements of data and code availability are available at https://doi.org/10.1038/s41594-020-00554-6.

Received: 11 August 2020; Accepted: 16 December 2020; Published online: 25 February 2021

References

- Griebel, G. & Holsboer, F. Neuropeptide receptor ligands as drugs for psychiatric diseases: the end of the beginning? *Nat. Rev. Drug Discov.* 11, 462–478 (2012).
- Shimada, I., Ueda, T., Kofuku, Y., Eddy, M. T. & Wüthrich, K. GPCR drug discovery: integrating solution NMR data with crystal and cryo-EM structures. *Nat. Rev. Drug Discov.* 18, 59–82 (2018).
- Hilger, D., Masureel, M. & Kobilka, B. K. Structure and dynamics of GPCR signaling complexes. Nat. Struct. Mol. Biol. 25, 4–12 (2018).
- Du, Y. et al. Assembly of a GPCR-G protein complex. Cell 177, 1232–1242 (2019).
- Qi, X. et al. Cryo-EM structure of oxysterol-bound human Smoothened coupled to a heterotrimeric G_i. Nature 571, 279–283 (2019).
- Rasmussen, S. G. F. et al. Crystal structure of the β2 adrenergic receptor-G_s protein complex. Nature 477, 549–557 (2011).
- Zhao, L.-H. et al. Structure and dynamics of the active human parathyroid hormone receptor-1. Science 364, 148–153 (2019).
- Kang, Y. et al. Cryo-EM structure of human rhodopsin bound to an inhibitory G protein. *Nature* 558, 553–558 (2018).
- Liang, Y. L. et al. Cryo-EM structure of the active, G_s-protein complexed, human CGRP receptor. Nature 561, 492–497 (2018).
- Liang, Y. L. et al. Phase-plate cryo-EM structure of a biased agonistbound human GLP-1 receptor—G_s complex. Nature 555, 121–125 (2018).
- García-Nafría, J., Lee, Y., Bai, X., Carpenter, B. & Tate, C. G. Cryo-EM structure of the adenosine A2A receptor coupled to an engineered heterotrimeric G protein. *Elife* 7, e35946 (2018).
- Kato, H. E. et al. Conformational transitions of a neurotensin receptor 1-G_{i1} complex. Nature 572, 80-85 (2019).
- García-Nafría, J., Nehmé, R., Edwards, P. C. & Tate, C. G. Cryo-EM structure of the serotonin 5-HT_{1B} receptor coupled to heterotrimeric G_o. Nature 558, 620–623 (2018).
- 14. Zhang, Y. et al. Cryo-EM structure of the activated GLP-1 receptor in complex with a G protein. *Nature* **546**, 248–253 (2017).
- Liang, Y. L. et al. Phase-plate cryo-EM structure of a class B GPCR-G-protein complex. Nature 546, 118–123 (2017).
- Draper-Joyce, C. J. et al. Structure of the adenosine-bound human adenosine A1 receptor-G_i complex. Nature 558, 559–563 (2018).
- 17. Koehl, \tilde{A} . et al. Structure of the μ -opioid receptor– G_i protein complex. *Nature* 558, 547–552 (2018).
- Krishna Kumar, K. et al. Structure of a signaling cannabinoid receptor 1–G protein complex. Cell 176, 448–458 (2019).
- 19. Yin, J. et al. Structure of a D2 dopamine receptor–G-protein complex in a lipid membrane. *Nature* **584**, 125–129 (2020).
- Lee, A. G. How lipids affect the activities of integral membrane proteins. Biochim. Biophys. Acta 1666, 62–87 (2004).
- Whorton, M. R. et al. Efficient coupling of transducin to monomeric rhodopsin in a phospholipid bilayer. J. Biol. Chem. 283, 4387–4394 (2008).
- Kofuku, Y. et al. Functional dynamics of deuterated β2-adrenergic receptor in lipid bilayers revealed by NMR spectroscopy. *Angew. Chem. Int. Ed.* 53, 13376–13379 (2014).
- 23. Strohman, M. J. et al. Local membrane charge regulates $\beta 2$ adrenergic receptor coupling to G_{i3} . Nat. Commun. 10, 2234 (2019).
- Yen, H.-Y. et al. PtdIns(4,5)P₂ stabilizes active states of GPCRs and enhances selectivity of G-protein coupling. *Nature* 559, 423–427 (2018).
- Inagaki, S. et al. Modulation of the interaction between neurotensin receptor NTS1 and Gq protein by lipid. J. Mol. Biol. 417, 95–111 (2012).
- Kitabgi, P. Targeting neurotensin receptors with agonists and antagonists for therapeutic purposes. Curr. Opin. Drug Discov. Devel. 5, 764–776 (2002).
- Nasr, M. L. et al. Covalently circularized nanodiscs for studying membrane proteins and viral entry. Nat. Methods 14, 49–52 (2016).
- 28. Wall, M. A. et al. The structure of the G protein heterotrimer $G_{in1}\beta_1\gamma_2$. Cell 83, 1047–1058 (1995).
- Egloff, P. et al. Structure of signaling-competent neurotensin receptor 1 obtained by directed evolution in *Escherichia coli. Proc. Natl Acad. Sci. USA* 111. E655–E662 (2014).

ARTICLES

- Ballesteros, J. A. & Weinstein, H. Integrated methods for the construction of three-dimensional models and computational probing of structurefunction relations in G protein-coupled receptors. *Methods Neurosci.* 25, 366–428 (1995).
- Knepp, A. M., Grunbeck, A., Banerjee, S., Sakmar, T. P. & Huber, T. Direct measurement of thermal stability of expressed CCR5 and stabilization by small molecule ligands. *Biochemistry* 50, 502–511 (2011).
- 32. Gao, Y. et al. Structures of the rhodopsin-transducin complex: insights into G-protein activation. *Mol. Cell* **75**, 781–790 (2019).
- Krumm, B. E., White, J. F., Shah, P. & Grisshammer, R. Structural prerequisites for G-protein activation by the neurotensin receptor. *Nat. Commun.* 6, 7895 (2015).
- Kim, H. R. et al. Structural mechanism underlying primary and secondary coupling between GPCRs and the Gi/o family. *Nat. Commun.* 11, 3160 (2020).
- 35. Huang, W. et al. Structure of the neurotensin receptor 1 in complex with β -arrestin 1. *Nature* **579**, 303–308 (2020).
- Liu, X. et al. Structural insights into the process of GPCR-G protein complex formation. Cell 177, 1243–1251 (2019).
- Dror, R. O. et al. Structural basis for nucleotide exchange in heterotrimeric G proteins. Science 348, 1361–1365 (2015).
- 38. Sun, X., Singh, S., Blumer, K. J. & Bowman, G. R. Simulation of spontaneous G protein activation reveals a new intermediate driving GDP unbinding. *Elife* 7, e38465 (2018).

- Chung, K. Y. et al. Conformational changes in the G protein G_s induced by the β2 adrenergic receptor. Nature 477, 611–617 (2011).
- Erlandson, S. C., McMahon, C. & Kruse, A. C. Structural basis for G protein-coupled receptor signaling. *Annu. Rev. Biophys.* 47, 1–18 (2018).
- Iiri, T., Bell, S. M., Baranski, T. J., Fujita, T. & Bourne, H. R. A G_{sa} mutant designed to inhibit receptor signaling through G_s. Proc. Natl Acad. Sci. USA 96, 499–504 (1999).
- Su, M. et al. Structural basis of the activation of heterotrimeric G_s-protein by isoproterenol-bound β1-adrenergic receptor. Mol. Cell 80, 59–71 (2020).
- Kaya, A. I. et al. A conserved phenylalanine as a relay between the α5 helix and the GDP binding region of heterotrimeric G_i protein α subunit. *J. Biol. Chem.* 289, 24475–24487 (2014).
- Sun, D. et al. Probing G_{ail} protein activation at single-amino acid resolution. Nat. Struct. Mol. Biol. 22, 686–694 (2015).
- 45. Flock, T. et al. Universal allosteric mechanism for $G\alpha$ activation by GPCRs. *Nature* **524**, 173–179 (2015).
- Goricanec, D. et al. Conformational dynamics of a G-protein α subunit is tightly regulated by nucleotide binding. *Proc. Natl Acad. Sci. USA* 113, E3629–E3638 (2016).

Publisher's note Springer Nature remains neutral with regard to jurisdictional claims in published maps and institutional affiliations.

© The Author(s), under exclusive licence to Springer Nature America, Inc. 2021

Methods

Circularized NDs. A plasmid expressing the NW9 membrane scaffolding protein is available through Addgene (133442) for academic/nonprofit institutions.

Preparation of NTSR1 in cNDs. Expression and purification of a thermostable variant of rat NTSR1 (TM86V-L167R ΔIC3B) was performed as described previously with some modifications^{29,47}. This NTSR1 variant consists of residues G50-G390, contains a deletion of E273-T290 in ICL3, and has 10 stabilizing mutations (Extended Data Fig. 1b). Briefly, the full-length fusion protein consisting of maltose-binding protein (MBP), NTSR1 and thioredoxin (TrxA) was expressed in Tuner (DE3) Competent Cells (Novagen) in LB medium at 37 °C, 200 r.p.m. and induced at an optical density at 600 nm of 0.75 with 1 mM IPTG. Cells were grown for another 24 h at 20 °C, 160 r.p.m. and collected by centrifugation (5,000g, 30 min, 4°C). Cells were then lysed and solubilized by sonication in buffer containing 100 mM HEPES (pH 8.0), 20% glycerol, 400 mM NaCl, 2.5 mM MgCl₂, 0.6/0.12% CHAPS/cholesterol, 1.7% n-decyl-β-D-maltopyranoside (DM), 100 mg lysozyme, one tablet of protease inhibitor and 250 U benzonase. The cell lysate was centrifuged, and the supernatant was mixed with pD-NTS resin (NTS coupled to sepharose resin through a fusion with a major part of protein D from phage lambda)⁴⁷ pre-equilibrated with 25 mM HEPES (pH 8.0), 10% glycerol, 600 mM NaCl and 0.5% DM at 4°C for 1 h. The flow-through from the pD-NTS resin was then discarded, and the resin was washed with 25 mM HEPES (pH 7.0), 10% glycerol, 150 mM NaCl, 2 mM DTT and 0.3% DM. The resin was then mixed with 3C protease for 1 h at 4°C to cleave off MBP and TrxA from NTSR1, as well as NTS-NTSR1 from pD resin⁴⁷. The resin was washed with 10 mM HEPES (pH7.0), 10% glycerol, 2 mM DTT and 0.3% DM, which was combined with the flow-through and loaded onto an SP cation exchange chromatography column (GE Healthcare) pre-equilibrated in the same washing buffer. The SP column was washed with 10 mM HEPES (pH 7.7), 10% glycerol, 35 mM NaCl, 2 mM DTT and 1% diheptanoylphosphatidylcholine (DH₇PC), then eluted with 10 mM HEPES (pH7.7), 10% glycerol, 350 mM NaCl, 2 mM DTT and 0.2% DH₇PC. The eluate was concentrated to below 500 µl and subjected to size-exclusion chromatography on a Superdex 200 10/300 Increase Analytical (S200a) column (GE Healthcare) equilibrated with 10 mM HEPES (pH7.7), 150 mM NaCl, 2 mM DTT, 0.1% DH₂PC and 0.1 μM NTS. Fractions containing NTSR1 were collected and mixed with a 3:2 molar ratio of POPC to POPG solubilized in 100 mM sodium cholate at a NTSR1:lipid molar ratio of 1:160. The mixture was incubated on ice for 30 min before addition of cNW9 at a cNW9:NTSR1 molar ratio of 4:1 followed by another 30 min of incubation on ice. The mixture was then treated with a 5% volume of Bio-Bead SM-2 resin (Bio-Rad) with shaking on ice for 15 min, followed by the addition of another 20% volume of Bio-Beads every 20 min for detergent removal. After 2h of incubation with Bio-Beads, the flow-through was then subjected to size-exclusion chromatography with an S200a column equilibrated in 20 mM sodium phosphate (pH 6.9), 50 mM NaCl, 1 mM DTT, 0.5 mM EDTA and 0.1 µM NTS. Fractions containing NTSR1-cND were concentrated to below 500 μl and incubated at 42 °C for 24 h, followed by filtration through 0.22-μm cutoff filters. The flow-through was subjected to another round of size-exclusion chromatography. Fractions were pooled, concentrated and stored at 4 °C.

Preparation of G α_{i1} β_1 γ_1 in micelles and cNDs. G protein composed of G α_{i1} , G β_1 and G γ_1 was expressed and purified as detailed previously^{29,48}. Briefly, *Spodoptera frugiperda* (Sf9) were grown in suspension in ESF921 medium (Expression Systems), infected at a density of 2 to $3 \times 10^6 \, \mathrm{ml}^{-1}$ with a single baculovirus encoding all three subunits (G α_{i1} β_1 γ_1), collected within 72 h post inoculation and stored at $-80\,^{\circ}\mathrm{C}$ until use.

Cells were lysed in 10 mM HEPES (pH7.4), 20 mM KCl, 10 mM MgCl₂, 10 μ M GDP, 2 mM β -mercaptoethanol (β -ME) and one protease inhibitor tablet with sonication. The suspension was then ultra-centrifuged at 180,000g for 45 min at 4 °C. The membrane pellet was solubilized in 50 mM HEPES (pH7.4), 150 mM NaCl, 10 mM MgCl₂, 10 μ M GDP, 2 mM β -ME, 10% glycerol, one protease inhibitor tablet, 1.2% DM at 4 °C for 3 h. The suspension was ultra-centrifuged again and the supernatant was purified through Ni-NTA resin. The eluate was concentrated and run through a Superdex 200 prep 16/60 column (S200p; GE Healthcare) equilibrated in 20 mM HEPES (pH7.4), 100 mM NaCl, 0.1 mM MgCl₂, 4 mM β -ME and 0.5% DM. Fractions containing $G\alpha_{i1}\beta_{i1}\gamma_{1}$ were pooled and concentrated to 10 mg ml⁻¹, flash-frozen in liquid nitrogen and stored at -80 °C.

 $G\alpha_{i1}\beta_i\gamma_i$ –cNDs were prepared in a similar manner as NTSR1–cNDs. After Bio-Bead removal, the $G\alpha_{i1}\beta_i\gamma_i$ –cNDs were purified through Ni-NTA to remove empty cNDs, followed by S200a chromatography to remove aggregates. Fractions containing pure $G\alpha_{i1}\beta_i\gamma_i$ –cNDs were collected, concentrated and stored at 4 °C.

Complex formation of NTS-NTSR1-G $\alpha_{ii}\beta_1\gamma_1$ in cNDs. Purified G $\alpha_{ii}\beta_1\gamma_1$ in micelles was diluted in buffer A (20 mM HEPES (pH 6.9), 50 mM NaCl, 5 mM CaCl₂, 1 mM DTT and 0.1 μ M NTS) until the DM concentration dropped below 0.08% (the critical micelle concentration of DM), then mixed with NTSR1-cND in a 1:1 molar ratio. The mixture was incubated on ice for 30 min, followed by addition of Bio-Beads at 10% volume every 30 min. The mixture was incubated on ice with shaking for a total of 2h and then the Bio-Beads were removed. Apyrase, diluted with buffer A and pretreated with Bio-Beads for 30 min on ice, was added

to the complex at $1~U~ml^{-1}$ concentration. The mixture was incubated at $4~^{\circ}C$ overnight, then subjected to an S200a size-exclusion column equilibrated in 20~mM sodium phosphate (pH 6.9), 50~mM NaCl, 1~mM DTT, 0.5~mM EDTA and $0.1~\mu M$ NTS. Peak fractions were characterized with SDS-PAGE and negative-stain EM. The fractions containing NTS-NTSR1-G $\alpha_{ii}\beta_{i}\gamma_{i}$ in cNDs were used for cryo-EM structure determination.

Circular dichroism spectroscopy. CD spectra were measured on a JASCO J-815 spectropolarimeter equipped with a Peltier cell temperature controller. Both spectrum scan measurements and variable-temperature measurements were carried out for the following samples: NTSR1 in DH₂PC micelles, NTSR1–cNDs, G $\alpha_{ii}\beta_1\gamma_1$ in DH₂PC micelles, $G\alpha_{ii}\beta_1\gamma_1$ -cNDs, NTSR1–G $\alpha_{ii}\beta_1\gamma_1$ in lauryl maltose neopentyl glycol (LMNG)/glyco-diosgenin (GDN)/cholesteryl hemisuccinate Tris salt (CHS) micelles (0.00375% LMNG, 0.00125% GDN and 0.000375% CHS) and NTSR1–G $\alpha_{ii}\beta_1\gamma_1$ in cNDs. Spectrum scan measurements were performed at 20 °C, before and after variable-temperature measurements, collecting data from 260 nm to 190 nm. Variable-temperature measurements were carried out at 220 nm on increasing the temperature from 20 °C to 95 °C at a rate of 1 °C min^-1. Spectrum Manager 2 software was used to analyze the transition temperature for each sample.

Binding affinity and kinetics measurement. The binding affinity and kinetics between NTSR1 and $G\alpha_n\beta_1\gamma_1$ in detergent micelles and cNDs were measured using MST and bio-layer interferometry.

For MST, the measurements were performed on a Monolith NT.115 system (NanoTemper Technologies). We measured the fluorescence signal from $G\alpha_{i1}\beta_1\gamma_1$ by using the Monolith His-Tag labeling kit RED-tris-NTA 2nd generation kit (NanoTemper Technologies). The samples were prepared in buffer containing 20 mM sodium phosphate (pH 6.9), 50 mM NaCl, 0.05% DH₇PC for cND titrations and 0.2% DH₇PC for titrations in detergent micelles. The concentration of DH₇PC for cND titrations is below its critical micellar concentration. The experiments were carried out as quickly as possible (within 1-2 min for sample preparation) to prevent degradation of $G\alpha_{i1}\beta_1\gamma_1$. The concentration of $G\alpha_{i1}\beta_1\gamma_1$ was constant at 10 nM. NTS-NTSR1 in DH₇PC, NTS-NTSR1-cND or empty cND was titrated in twofold dilution steps beginning at $4\,\mu\text{M}.$ For measurements, the samples were filled into premium-coated capillaries. Measurements were performed at 2% light-emitting diode (LED) and 20% MST power, 30 s laser on and 5 s laser off. Fluorescence was excited at 605-645 nm and emission was detected at $680-685\,\mathrm{nm}$. The results were analyzed using MO Affinity Analysis software (NanoTemper Technologies). The dissociation constant (K_d) was then determined using a single-site model for data fitting. Two independent biological samples were used for measurements in POPC/POPG (3/2) cNDs, detergent micelles, POPC cNDs, POPG cNDs and the alanine mutant TM86V-L167R (E66A/K176A/ K178A/S182A/R185A) in POPC/POPG (3/2) cNDs, each with three technical repeats. One biological sample was used for measurements in POPC/POPG/CHS (3/2/0.3) cNDs with three technical repeats. Two biological samples were used for measurement in empty POPC/POPG (3/2) cNDs.

Bio-layer interferometry experiments were performed on an Octet RED384 system (ForteBio) using anti-His antibody-coated Dip and Read Biosensors (HIS1, ForteBio) and 384-well plates (ForteBio) with 60-µl volume. His-tagged $G\alpha_{i1}\beta_1\gamma_1$ (500 nM) was bound for 5 min in binding buffer consisting of 20 mM HEPES (pH 7.4), 100 mM NaCl, 0.1 mM MgCl $_2$, 4 mM β -ME and 0.5% DM. To test for non-specific binding of His-tagged $G\alpha_{ii}\beta_i\gamma_i$, reference tips were incubated in buffer alone. The tips were washed with buffer for 2 min to obtain a baseline reading and then transferred to wells in various concentrations of NTS-NTSR1cND (4, 2, 1, 0.5 and 0.25 μM) in buffer containing 20 mM sodium phosphate (pH 6.9), 50 mM NaCl, 1 mM DTT, 0.5 mM EDTA and 0.1 μM NT for 5 min. After measuring the association phase, tips were moved to wells containing buffer with and without GTPγS, and dissociation was measured for 5 min. The data were processed and analyzed using the Octet data analysis software, version 11.0 (ForteBio). Association-dissociation curves for each concentration were fit to a 2:1 model. Three independent biological samples were used for the measurement of NTSR1-Gi binding in cNDs. Two independent biological samples were used for the measurement of GTPyS dissociation and empty cND-Gi binding.

Nuclear magnetic resonance spectroscopy. Uniformly ^{15}N -labeled NTS–NTSR1 in POPC/POPG (3:2) cNW9 NDs at 200 μM , alone and in complex with unlabeled $G\alpha_{ii}\beta_i\gamma_i$ at a molar ratio of 5:1, were prepared as described above in NMR buffer (20 mM sodium phosphate (pH6.9), 50 mM NaCl, 1 mM DTT, 0.5 mM EDTA and 10% D₂O). Two-dimensional transverse relaxation optimized spectroscopy (TROSY) heteronuclear single quantum coherence (HSQC) data were collected with 2,000 scans in 200 increments at 45 °C on a Bruker 800-MHz spectrometer equipped with a TXO cryogenic probe. TROSY HSQC measurements were repeated for NTS–NTSR1–cND on an Agilent 700-MHz spectrometer to verify that the NTS–NTSR1–cND stays intact after long data acquisition in the magnet at 45 °C. Data were processed using the NMRPipe software package 49 .

Functional assay. Ligand-induced IP1 accumulation was measured in transiently transfected HEK293T/17 cells as described before⁵⁰. Wild-type rat NTSR1 or

mutants thereof were directly subcloned into a mammalian expression vector containing an N-terminal SNAP-tag (pMC08). At 24h after transfection, cells were washed with PBS, detached with trypsin-EDTA (Sigma) and resuspended in assay buffer (10 mM HEPES pH 7.4, 1 mM CaCl₂, 0.5 mM MgCl₂, 4.2 mM KCl, 146 mM NaCl, 50 mM LiCl, 5.5 mM glucose and 0.1% (wt/vol) BSA). Cells were seeded at 20,000 cells per well in white 384-well plates (Greiner) and incubated for 2h at 37 °C with a concentration range of NTS₈₋₁₃ (Anawa) diluted in assay buffer. IP1 accumulation was measured using the HTRF IP-One kit (Cisbio) according to the manufacturer's protocol. To confirm cell surface expression of NTSR1 and its mutants, transfected cells were plated on poly-D-lysine-treated 384-well plates (Greiner) at 20,000 cells per well in growth medium. The following day, medium was removed and cells were incubated with 50 nM SNAP-Lumi4-Tb (CisBio) in labeling buffer (CisBio) for 2 h at 37 °C. Thereafter, cells were washed four times with wash buffer (20 mM HEPES pH 7.5, 100 mM NaCl, 3 mM MgCl, and 0.2% (wt/vol) nonfat milk). The fluorescence intensity of Tb3+-labeled receptors was measured on an Infinite M1000 fluorescence plate reader (Tecan) with an excitation wavelength of 340 nm and emission wavelength of 620 nm. To generate concentration-response curves, data were normalized to receptor expression at the cell surface and to the response of NTSR1 at maximal ligand concentration and were analyzed by a nonlinear curve fit in GraphPad Prism.

Negative-stain electron microscopy. NTS-NTSR1- $G\alpha_{il}\beta_i\gamma_i$ -cND complex $(3\,\mu l)$ at a concentration of $0.02\,mg\,ml^{-1}$ was applied onto a glow-discharged continuous carbon grid (Electron Microscopy Sciences). After 2 min of adsorption, the grid was blotted with filter paper to remove the excess sample, immediately washed twice with $50\,\mu l$ of MilliQ water, once with $50\,\mu l$ of 0.75% uranyl formate solution and incubated with $50\,\mu l$ of 0.75% uranyl formate solution for an additional 1 min. The grid was then further blotted with filter paper followed by vacuum aspiration to remove excess stain, and finally examined with a Tecnai T12 electron microscope (Thermo Fisher Scientific) equipped with an LaB6 filament and operated at an acceleration voltage of $120\,kV$, using a nominal magnification of $\times 52,000$ at a pixel size of $2.13\,\text{Å}$.

Cryo-electron microscopy sample preparation. Cryo-EM grids were prepared using a Vitrobot Mark IV system (Thermo Fisher Scientific). NTS–NTSR1–G $\alpha_i\beta_i\gamma_i$ –cND (3 µl), at a concentration between 1.5 mg ml $^{-1}$ and 1.7 mg ml $^{-1}$, was applied onto glow-discharged C-flat holey carbon grids (R1.2/1.3, 400 mesh copper, Electron Microscopy Sciences) or Quantifoil holey carbon grids (R1.2/1.3, 400 mesh gold, Quantifoil Micro Tools). The grids were blotted for 7.5s with a blot force of 16 and 100% humidity before being plunged into liquid ethane cooled by liquid nitrogen.

Cryo-electron microscopy data collection. Images of NTS–NTSR1–G $\alpha_n \beta_1 \gamma_1$ –cND were acquired on a Titan Krios I microscope (Harvard Cryo-EM Center for Structural Biology) equipped with a BioQuantum K3 imaging filter (slit width of 20 eV) and a K3 direct electron detector (Gatan) and operating at an acceleration voltage of 300 kV. Images were recorded at a defocus range of $-1.2\,\mu m$ to $-2.5\,\mu m$ with a nominal magnification of $\times 105,000$, resulting in a pixel size of 0.825 Å. Each image was dose-fractionated into 38 video frames with a total exposure time of 1.5 s, resulting in a total dose of $\sim \!\! 57$ electrons per Å 2 . SerialEM software was used for data collection $^{\rm s1}$.

Image processing. A total of 23,677 video stacks, which were collected during two sessions, were motion-corrected and electron-dose-weighted using MotionCor2 (ref. ⁵²). Parameters of the contrast transfer function (CTF) were estimated from the motion-corrected micrographs using CTFFIND4 (ref. ⁵³). To generate a reference, particles from 10 micrographs were picked manually in EMAN2.2 (ref. ⁵⁴), and crYOLO⁵⁵ was then trained for picking particles automatically. All subsequent 2D and 3D analyses were performed using RELION-3.0 or RELION-3.1-beta ⁵⁶.

A total of 1,726,457 particles were selected after several rounds of 2D classification from 4,367,542 autopicked particles. The density map of the human NTSR1 in complex with the agonist JMV449 and the heterotrimeric G_{ii} protein (EMDB-20180) 12 was low-pass-filtered to 20 Å and used as the initial model for the first round of 3D classification, yielding five different classes. Two classes of the NTS-NTSR1- $G\alpha_{ii}\beta_{i}\gamma_{i}$ -cND complex were relatively better resolved and particles from these two classes were subject to 3D refinements. Bayesian polishing was then performed, followed by 3D refinement and post-processing, yielding two density maps at resolutions of 4.3 Å (canonical state) and 4.5 Å (noncanonical state). To further improve the resolution of the core of the complex, masks excluding the ND and the AHD were applied during the 3D refinement, yielding the 4.1-Å (canonical state) and 4.2-Å (noncanonical state) density maps, respectively. Per-particle CTF refinement was performed but did not lead to an improvement in map resolution or quality.

Model building and refinement. The crystal structures of the NTS-NTSR1 complex (PDB 4BUO)²⁹ and G-protein heterotrimer $G\alpha_{i1}\beta_{i1}\gamma_{2}$ (PDB 1GP2)²⁸ and the cryo-EM structure of $G\alpha_{7}\beta_{1}\gamma_{1}$ (PDB 6OY9)³² were fitted into the density map of the canonical NTS-NTSR1- $G\alpha_{i1}\beta_{1}\gamma_{1}$ -cND complex using the Fit in Map function of Chimera⁵⁷. The $\alpha_{i1}\beta_{1}$ subunits of $G\alpha_{i1}\beta_{1}\gamma_{2}$ and the γ_{1} subunit of $G\alpha_{7}\beta_{1}\gamma_{1}$ were merged with the NTS-NTSR1 structure and the amino acids were modified in Coot version 0.9-pre to match our constructs⁵⁸. The amino acids N292–R299

of NTSR1 of the canonical state were mutated to poly-alanine due to the lack of side chain densities. The model was manually adjusted and refined in Coot with torsion, planar peptide, trans peptide and Ramachandran restraints applied. For the noncanonical state, the subunits of the refined atomic model of the canonical state were fitted into the density map as separate rigid bodies. The model was manually adjusted and refined in Coot. For both states, the AHD was extracted from the crystal structure of the human $G\alpha_{i1}$ (PDB 3UMR) and docked into the density as a rigid body using Chimera.

Models were refined with Phenix.real_space_refine⁵⁹. The AHD was not refined due to a lack of side chain information for this domain. During refinement, the resolution limit was set to match the map resolution determined by the FSC=0.143 criterion in post-processing. Secondary structure, Ramachandran, rotamer and reference restraints from the JMV449–NTSR1– G_i -scFv16 model (PDB 6OS9)¹² were applied throughout refinement. The final models were validated using MolProbity v.4.3.1 (ref. ⁶⁰) with the model statistics provided in Table 1.

Molecular dynamics simulations. The molecular system for the molecular dynamics simulations was prepared based on the canonical state structure of NTS-NTSR1-G $\alpha_n\beta_1\gamma_1$ -cND, which was pre-processed with Maestro from Schrödinger^{61,62}. Bond orders were assigned, hydrogens added, disulfide bonds created and het states generated at pH7.0 \pm 2.0. The side chains of residues 291–299 were assigned and the truncated residues 273–290 in the NTSR1 construct were added with the Crosslink Proteins tool of Maestro^{61,62}.

The membrane and solvent environment, as well as the input files for Amber, were generated using the Membrane Builder tool of CHARMM-GUI 63,64 . The terminal groups of each chain were patched with standard N terminus and C terminus patch residues, except for the N terminus of G α , for which a GLYP patch residue was used. For orienting the complex appropriately, the PPM (Positioning of Proteins in Membrane) server of the OPM (Orientations of Proteins in Membranes) database was used 65 . A lipid bilayer containing a total of 527 lipids, composed of a 3:2 molar ratio of POPC to POPG, was added to the aligned complex with Membrane Builder 63,64 . A rectangular solvation box was added by adding water layers of at least 22.5 Å above and below the membrane. The system was ionized and neutralized by adding 50 mM of sodium and chloride ions. The resulting system contained a total of 286,109 atoms.

In total, 12 simulations of the prepared system were run using Amber18 (ref. 66). The Amber FF14SB⁶⁷ and Amber Lipid17 (ref. 68) force fields were used for the proteins and the lipid bilayer, respectively. The TIP3P model⁶⁰ was used for the water molecules. During the energy minimization, 2,500 steps of steepest descent followed by 2,500 steps of conjugate gradient were carried out. The equilibration steps were carried out according to the standard Membrane Builder protocols⁷⁰. The production MD simulations were carried out at 310 K and 1 bar in an NPT ensemble using a Monte Carlo barostat and a Langevin thermostat. The cutoff for the non-bonded interactions was set to 10 Å, and the particle mesh Ewald method was used for long-range electrostatic interactions. Hydrogen mass repartitioning was enabled and a time step of 4fs applied. Post-processing was carried out with AmberTools 18 and VMD 1.9.4 (ref. 66) The simulation lengths of the runs were between 600 ns and 1 us.

Reporting Summary. Further information on research design is available in the Nature Research Reporting Summary linked to this Article.

Data availability

EM density maps and atomic models of the NTS-NTSR1- G_i complex in lipid nanodiscs have been deposited in the Electron Microscopy Data Bank (EMDB) and wwPDB, respectively, under accession codes EMD-23099 and PDB 7L0P (canonical state without AHD), EMD-23100 and PDB 7L0Q (canonical state with AHD), EMD-23101 and PDB 7L0R (noncanonical state without AHD) and EMD-23102 and PDB 7L0S (noncanonical state with AHD).

References

- Egloff, P., Deluigi, M., Heine, P., Balada, S. & Plückthun, A. A cleavable ligand column for the rapid isolation of large quantities of homogeneous and functional neurotensin receptor 1 variants from *E. coli. Protein Expr. Purif.* 108, 106–114 (2015).
- Hillenbrand, M., Schori, C., Schöppe, J. & Plückthun, A. Comprehensive analysis of heterotrimeric G-protein complex diversity and their interactions with GPCRs in solution. *Proc. Natl Acad. Sci. USA* 112, E1181–E1190 (2015).
- Delaglio, F. et al. NMRPipe: a multidimensional spectral processing system based on UNIX pipes. J. Biomol. NMR 6, 277–293 (1995).
- Ehrenmann, J. et al. High-resolution crystal structure of parathyroid hormone 1 receptor in complex with a peptide agonist. *Nat. Struct. Mol. Biol.* 25, 1086–1092 (2018).
- Schorb, M., Haberbosch, I., Hagen, W. J. H., Schwab, Y. & Mastronarde, D. N. Software tools for automated transmission electron microscopy. *Nat. Methods* 16, 471–477 (2019).
- Zheng, S. Q. et al. MotionCor2: anisotropic correction of beam-induced motion for improved cryo-electron microscopy. Nat. Methods 14, 331–332 (2017).

- Rohou, A. & Grigorieff, N. CTFFIND4: fast and accurate defocus estimation from electron micrographs. J. Struct. Biol. 192, 216–221 (2015).
- Tang, G. et al. EMAN2: an extensible image processing suite for electron microscopy. J. Struct. Biol. 157, 38–46 (2007).
- 55. Wagner, T. et al. SPHIRE-crYOLO is a fast and accurate fully automated particle picker for cryo-EM. *Commun. Biol* **2**, 218 (2019).
- Zivanov, J. et al. New tools for automated high-resolution cryo-EM structure determination in RELION-3. Elife 7, e42166 (2018).
- Pettersen, E. F. et al. UCSF Chimera—a visualization system for exploratory research and analysis. *J. Comput. Chem.* 25, 1605–1612 (2004).
- Emsley, P. & Cowtan, K. Coot: model-building tools for molecular graphics. *Acta Crystallogr. D Biol. Crystallogr.* 60, 2126–2132 (2004).
- Afonine, P. V. et al. Real-space refinement in PHENIX for cryo-EM and crystallography. Acta Crystallogr. D Struct. Biol. 74, 531–544 (2018).
- 60. Williams, C. J. et al. MolProbity: more and better reference data for improved all-atom structure validation. *Protein Sci.* 27, 293–315 (2018).
- 61. Schrödinger Suite 2018-2 Protein Preparation Wizard (Schrödinger, 2019).
- Madhavi Sastry, G., Adzhigirey, M., Day, T., Annabhimoju, R. & Sherman, W. Protein and ligand preparation: parameters, protocols and influence on virtual screening enrichments. J. Comput. Aided Mol. Des. 27, 221–234 (2013).
- Jo, S., Kim, T., Iyer, V. G. & Im, W. CHARMM-GUI: a web-based graphical user interface for CHARMM. J. Comput. Chem. 29, 1859–1865 (2008).
- Lee, J. et al. CHARMM-GUI Membrane Builder for complex biological membrane simulations with glycolipids and lipoglycans. J. Chem. Theory Comput. 15, 775–786 (2019).
- Lomize, M. A., Pogozheva, I. D., Joo, H., Mosberg, H. I. & Lomize, A. L. OPM database and PPM web server: resources for positioning of proteins in membranes. *Nucleic Acids Res* 40, D370–D376 (2012).
- 66. Case, D. A. et al. AMBER 2018 (University of California, San Francisco, 2018).
- Maier, J. A. et al. ff14SB: improving the accuracy of protein side chain and backbone parameters from ff99SB. J. Chem. Theory Comput. 11, 3696–3713 (2015).
- Dickson, C. J. et al. Lipid14: the amber lipid force field. J. Chem. Theory Comput. 10, 865–879 (2014).
- Jorgensen, W. L., Chandrasekhar, J., Madura, J. D., Impey, R. W. & Klein, M. L. Comparison of simple potential functions for simulating liquid water. J. Chem. Phys. 79, 926–935 (1983).
- Lee, J. et al. CHARMM-GUI input generator for NAMD, GROMACS, AMBER, OpenMM and CHARMM/OpenMM simulations using the CHARMM36 additive force field. J. Chem. Theory Comput. 12, 405–413 (2016).

Acknowledgements

Cryo-EM data were collected at the Harvard Cryo-Electron Microscopy Center for Structural Biology. We thank F. Koh, P. Egloff, P. Heine, M. Hillenbrand and J. Schöppe

for their contribution to the early stages of this project; S. Sterling, R. Walsh and Z. Li for microscopy support; SBGrid for computing support; M. Deluigi for supervising the signaling experiments; and R. Walker, K. Bayer, P. Imhof and M. Bagherpoor for their advice and discussions regarding the molecular dynamics simulations. M.Z. is supported by a Charles Robert Broderick III Phytocannabinoid Research Fellowship. M.G. is supported by a Merck-BCMP fellowship. A.B. is supported by the International Retinal Research Foundation, the E. Matilda Ziegler Foundation for the Blind, the Richard and Susan Smith Family Foundation and the Pew Charitable Trusts. We acknowledge support from NIH grants GM129026 and Al037581 to G.W. and GM131401 to M.L.N. G.W. and A.P. are supported by HFSP RGP0060/2016. A.P. is supported by Swiss National Science Foundation grant no. 31003A_182334.

Author contributions

M.Z. developed the protocol for making NTS-NTSR1- $G\alpha_{i1}\beta_1\gamma_1$ -cND complexes, prepared samples, collected negative-stain EM images and performed biophysical experiments. M.G. prepared cryo-EM grids, obtained and processed the data, and built and refined the atomic models. M.Z. and Z.-F.W. performed binding experiments. C.G. performed MD simulations. J.J.Y. expressed $G\alpha_{i1}\beta_1\gamma_1$. H.W. obtained and processed cryo-EM data. M.Z. and Z.-y.S. performed NMR experiments. C.K., L. Merklinger and L. Morstein made constructs and performed signaling experiments. A.P. designed and supervised the signaling experiments. F.H. and G.W. initiated the project. A.B., M.L.N. and G.W. designed and supervised the project. M.Z. wrote the manuscript. M.Z., M.G., Z.-F.W., C.G., J.J.Y., C.K., A.P., A.B., M.L.N. and G.W. edited the manuscript.

Competing interests

M.L.N. and G.W. founded the company NOW Scientific to sell assembled cNDs. The other authors declare no competing interests.

Additional information

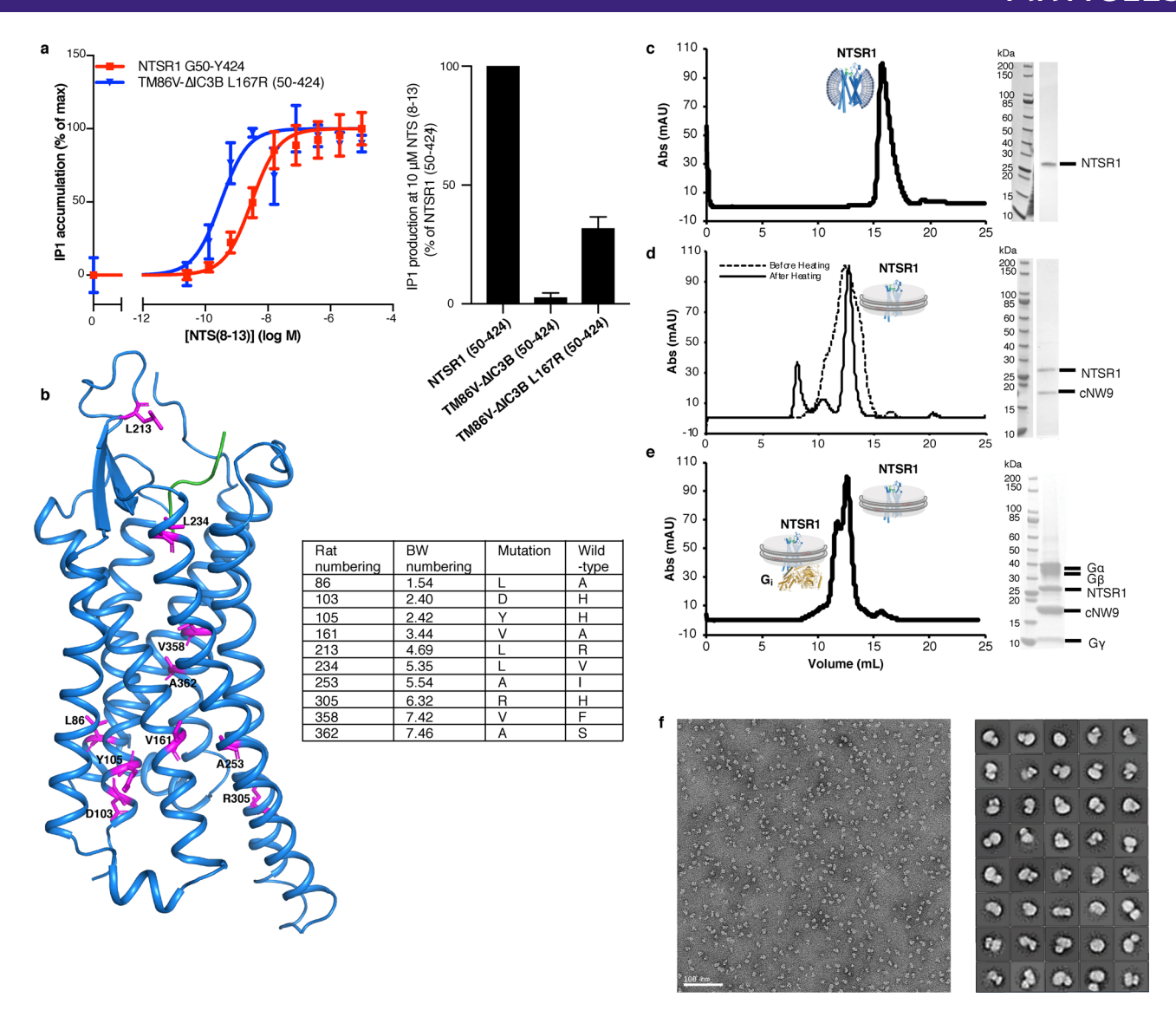
Extended data is available for this paper at https://doi.org/10.1038/s41594-020-00554-6.

Supplementary information The online version contains supplementary material available at https://doi.org/10.1038/s41594-020-00554-6.

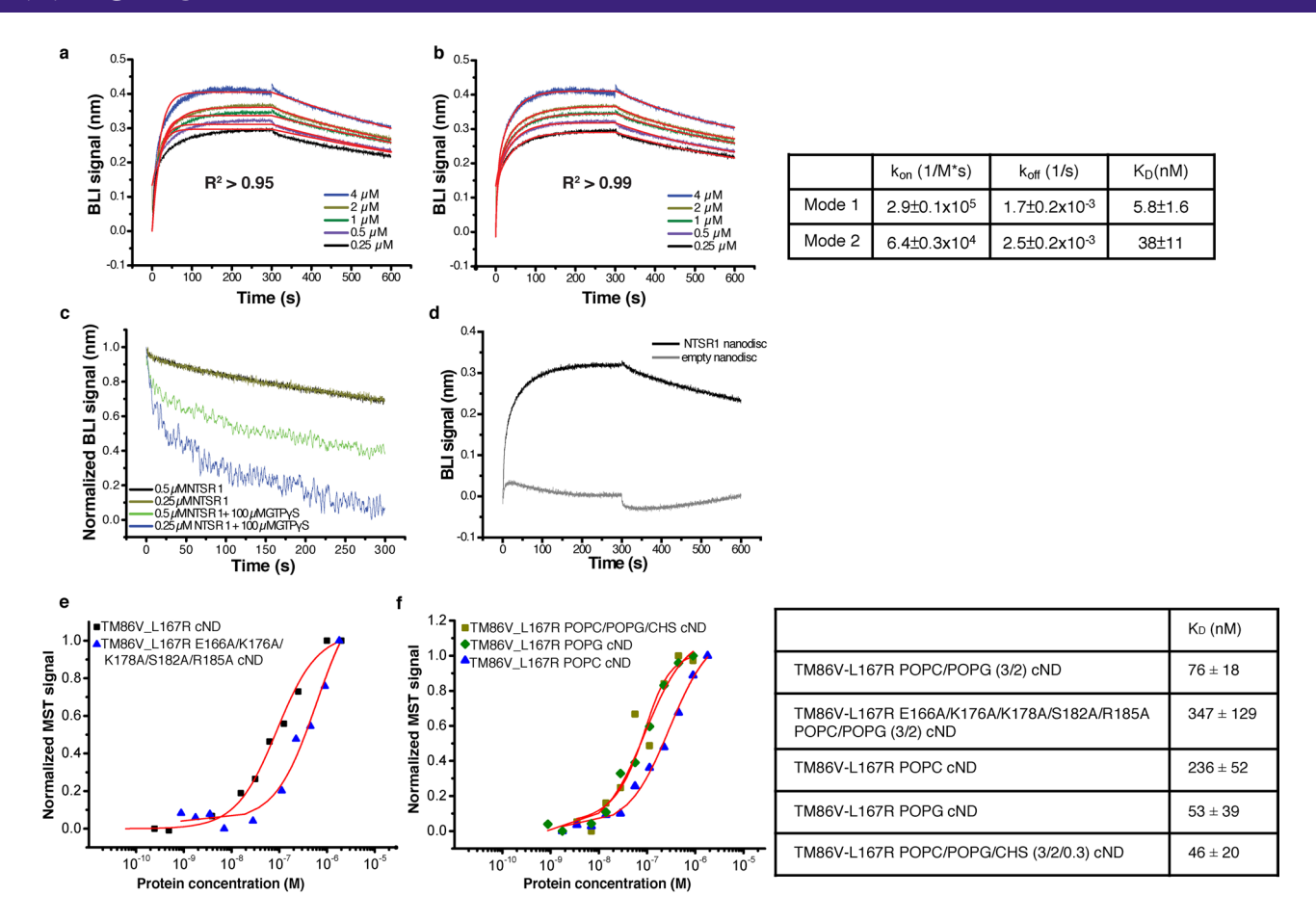
Correspondence and requests for materials should be addressed to A.B., M.L.N. or G.W

Peer review information Nature Structural & Molecular Biology thanks Ka Young Chung, Arun Shukla and the other, anonymous, reviewer(s) for their contribution to the peer review of this work. Inês Chen was the primary editor on this article and managed its editorial process and peer review in collaboration with the rest of the editorial team.

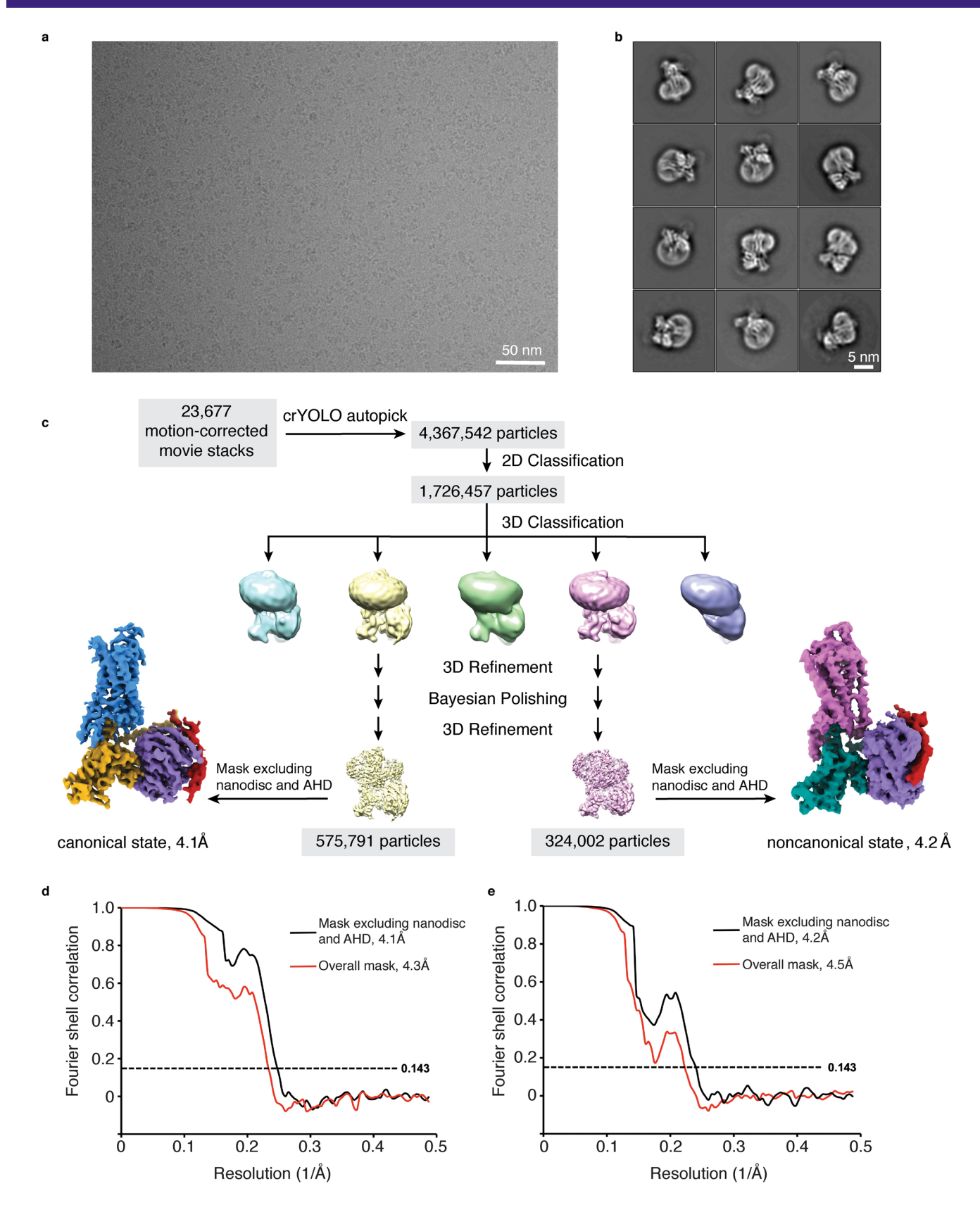
Reprints and permissions information is available at www.nature.com/reprints.



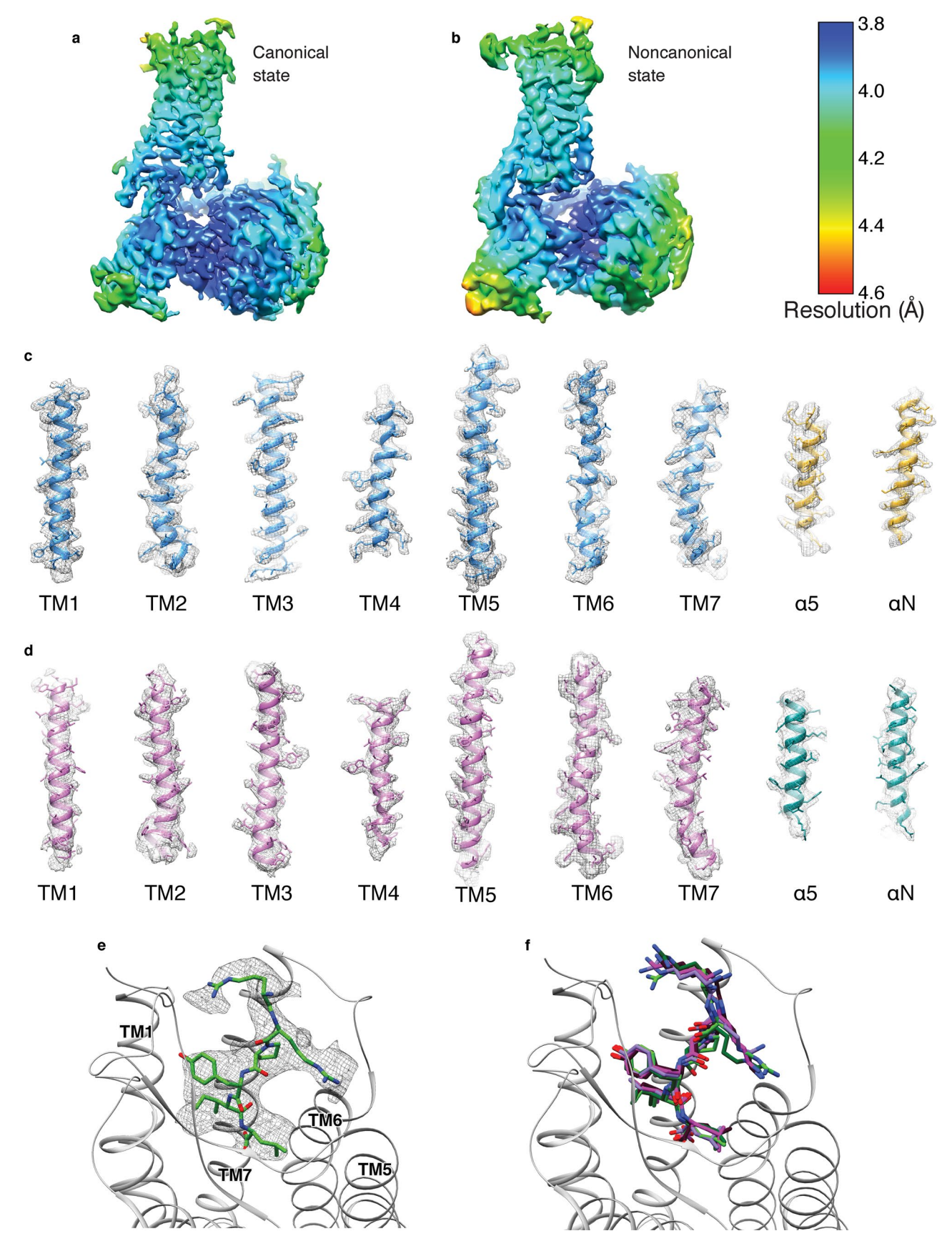
Extended Data Fig. 1 | Signaling competency and preparation of NTS-NTSR1-Gi complex in cNDs. a, Signaling competency of NTSR1 constructs. Wild-type NTSR1 (50-424) or NTSR1 variants were transiently transfected into HEK293T/17 cells, and activation of $Gα_q$ signaling was quantified by measuring inositol-1-phosphate (IP1) accumulation after stimulation with NTS₈₋₁₃. Data were normalized to receptor expression at the cell surface and are shown as mean and s.e.m. of n = 4 independent experiments (each performed in duplicate). Left, dose dependent IP1 production expressed as percentage of IP1 accumulation at maximal ligand concentration. Fitting of the curves result in EC50 of 2.7 nM for wild-type NTSR1 and 0.22 nM for TM86V ΔIC3B L167R. Right, bar graph showing IP1 production level at 10 μM agonist NTS₈₋₁₃. The NTSR1 variant TM86V ΔIC3B lacking the L167R back mutation exhibits no IP1 production, suggesting a critical role of R167^{3.50} in signal transduction. **b**, Residues mutated in the TM86V-L167R construct shown as magenta sticks on the left and listed in the table on the right. **c-e**, Size-exclusion chromatograms and corresponding SDS-PAGE gels for (**c**) NTSR1 in DH₇PC detergent micelles, (**d**) NTSR1 in POPC/POPG cNW9 nanodiscs before (dashed line) and after (solid line) heating, and (**e**) NTSR1-G_i complex in POPC/POPG cNW9 nanodiscs. **f**, Fractions corresponding to the NTS-NTSR1-G_i complex in (**e**) were analyzed by negative-stain EM, and then used for cryo-EM structure determination. Left, representative negative-stain EM micrograph of NTS-NTSR1-G_i complexes in cNDs. Right, 2D class averages.



Extended Data Fig. 2 | Characterization of the binding kinetics between NTS-NTSR1 and G_i in cNDs. a-b, Fitting of Bio-Layer Interferometry (BLI) traces of G_i binding to NTS-NTSR1-cND using (**a**) one binding mode and (**b**) two binding mode shows better fitting using two binding mode. Right, a table showing k_{onr} k_{off} and K_D from the two binding mode fitting. **c**, Dissociation between G_i and NTS-NTSR1-cND in the absence (black and brown) and presence (green and blue) of GTPγS, showing faster dissociation of the complex in the presence of GTPγS, suggesting that the NTSR1-Gα_{ii}β_iγ₁ complex in cNDs is capable of GDP/GTP exchange. **d**, Association and dissociation kinetics of G_i binding to NTS-NTSR1-cND (dark) and empty cND (gray), showing much slower association and faster dissociation of G_i binding to empty cND compared to NTS-NTSR1-cND, suggesting that interaction between G_i and NTS-NTSR1-cND is driven by G_i binding to NTSR1 rather than to the nanodisc. **e**, Microscale thermophoresis (MST) data for the binding between NTSR1 and G_i (square mark), as well as the binding between mutant TM86V-L167R E166A/K176A/K178A/S182A/R185A and G_i (triangle mark) in POPC/POPG (3/2) cND. **f**, MST data for the binding between NTSR1 and G_i in POPC cND (triangle mark), POPG cND (diamond mark) and POPC/POPG/CHS cND (square mark). Right, a table showing K_D from **e-f**.



Extended Data Fig. 3 | Cryo-EM data processing. a, Representative micrograph showing the distribution of NTS-NTSR1-G_i-cND particles in vitreous ice. **b**, Selected two-dimensional class averages showing secondary structure features. The cND has an approximate diameter of 9 nm. **c**, Simplified flow chart of the cryo-EM processing. Two datasets were collected and processed similarly; the number of particles shown here are a conflation of both datasets. Two well-resolved classes corresponding to canonical and noncanonical states were identified. Further rounds of classification did not identify additional classes or improve the resolution or map quality. **d,e**, Fourier shell correlation (FSC) curves for the (**d**) canonical state and (**e**) noncanonical state with masks that either include or exclude the cND and AHD.

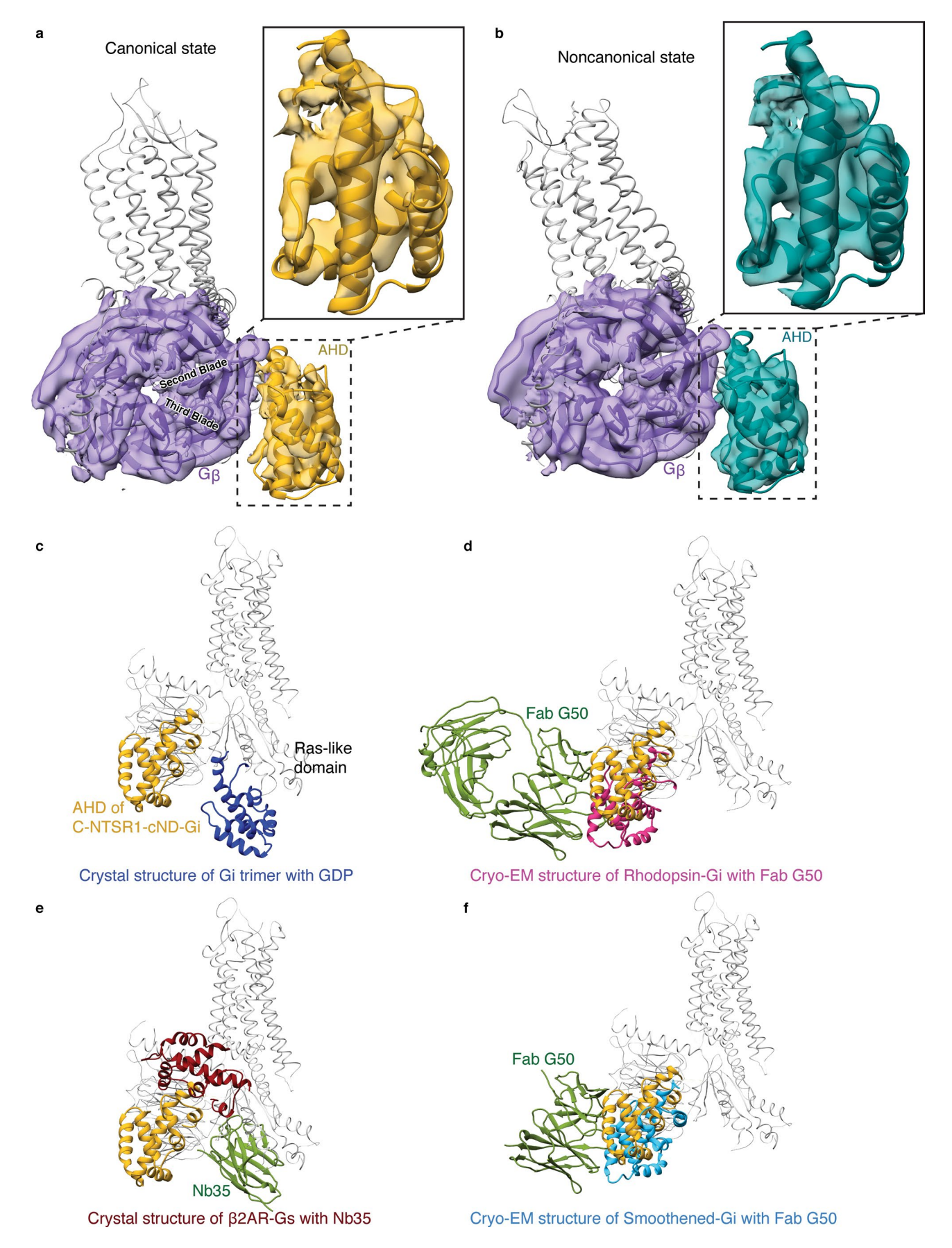


Extended Data Fig. 4 | See next page for caption.

NATURE STRUCTURAL & MOLECULAR BIOLOGY

ARTICLES

Extended Data Fig. 4 | Cryo-EM density. a,b, Local resolution of the NTS-NTSR1- G_1 complex in the (a) canonical state and (b) noncanonical state. The local resolution was calculated in RELION-3. c,d, Density and model for the transmembrane helices of NTSR1 and the α 5 and α N-helices of $G\alpha_{11}$ in the (c) canonical state and (d) noncanonical state. e, Density and model for NTS₈₋₁₃. f, Superposition of the atomic models of NTS₈₋₁₃ from the NTS-NTSR1- G_1 -cND complex in the canonical (light green), and noncanonical state (dark green) with NTS from the NTS-NTSR1 crystal structure (purple; PDB 4XEE) and JMV449 (an NTS analog) from the NTSR1- G_1 -detergent complex in the canonical (magenta; PDB 6OS9) and noncanonical state (dark red; PDB 6OSA).

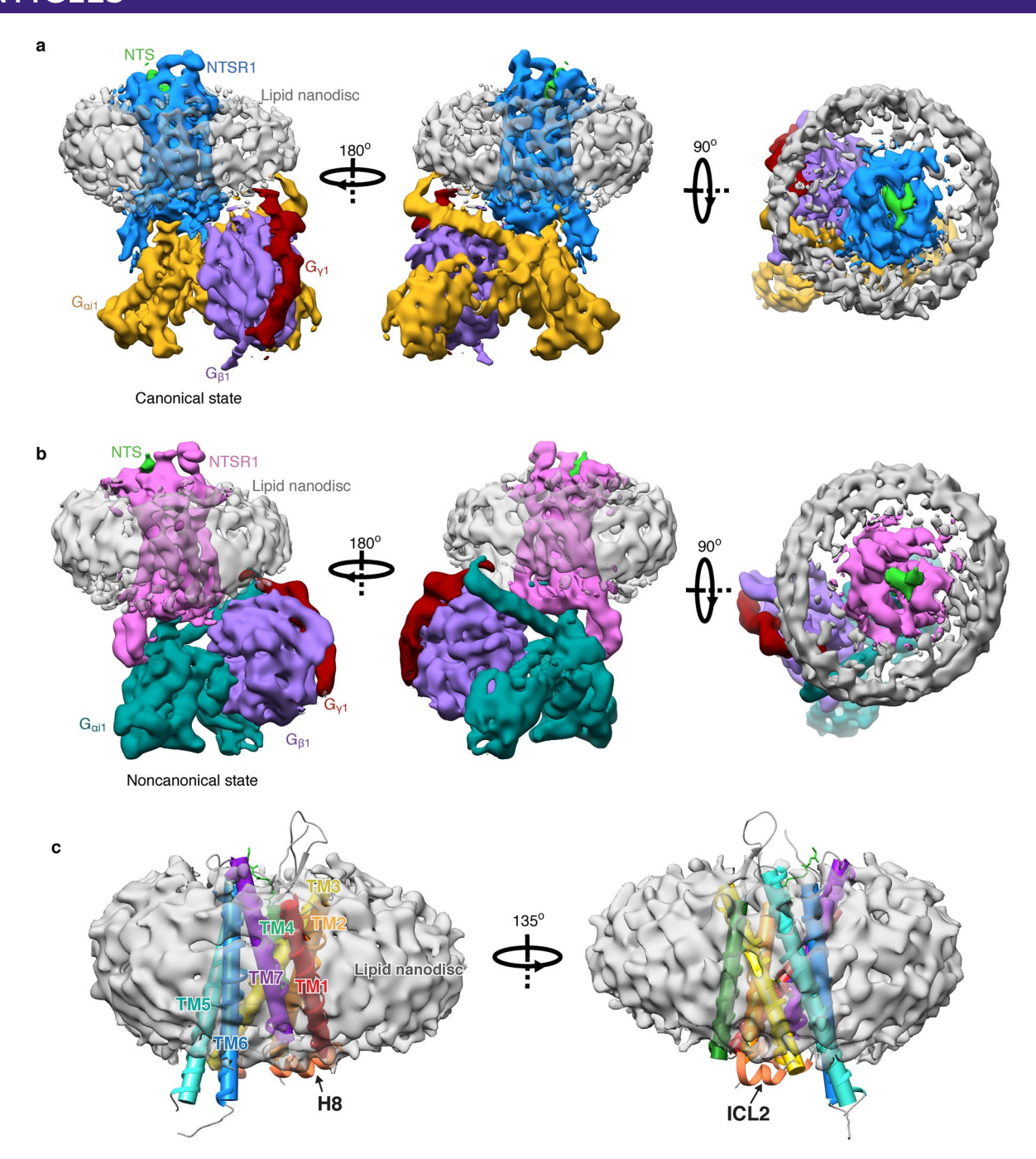


Extended Data Fig. 5 | See next page for caption.

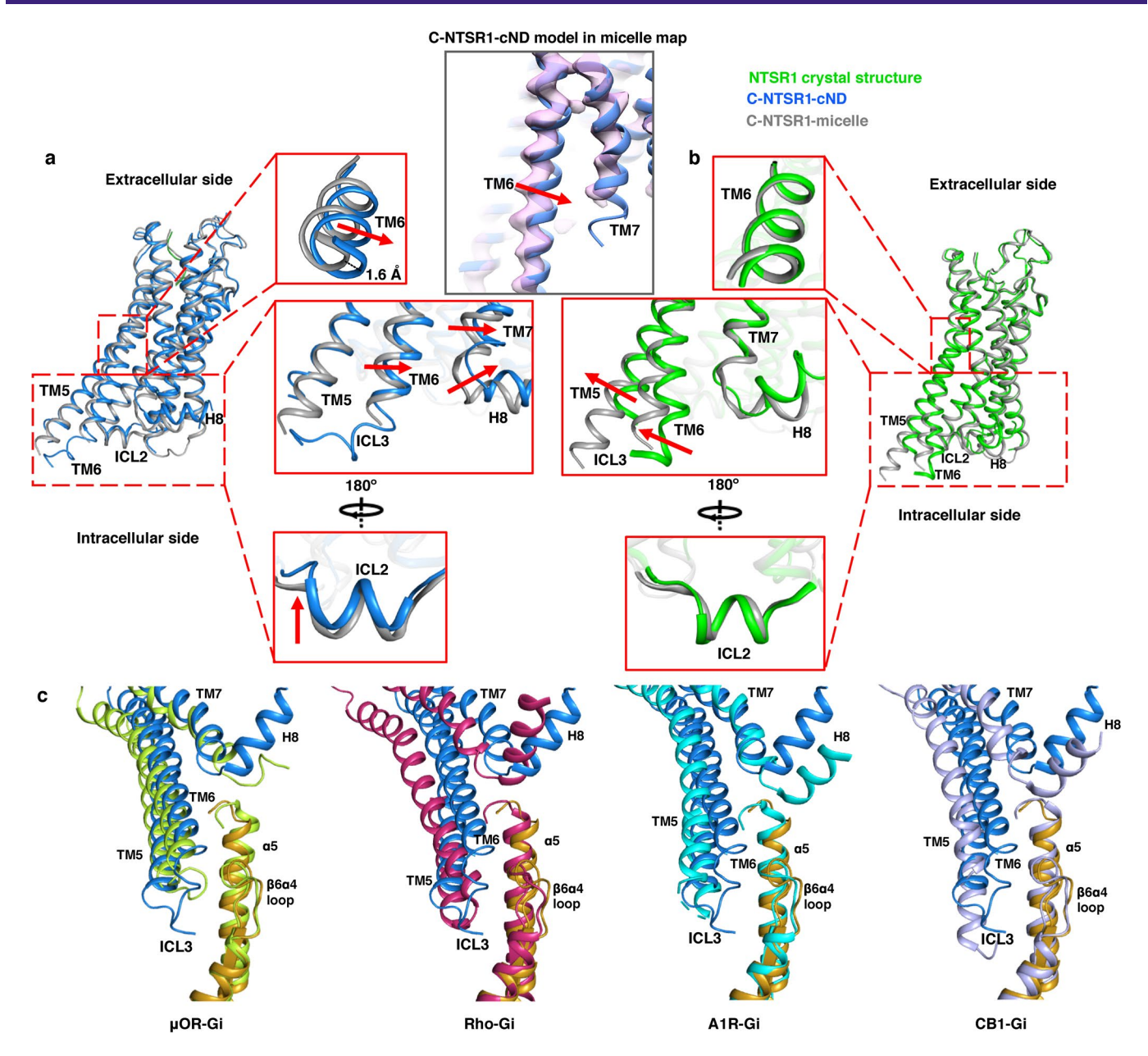
NATURE STRUCTURAL & MOLECULAR BIOLOGY

ARTICLES

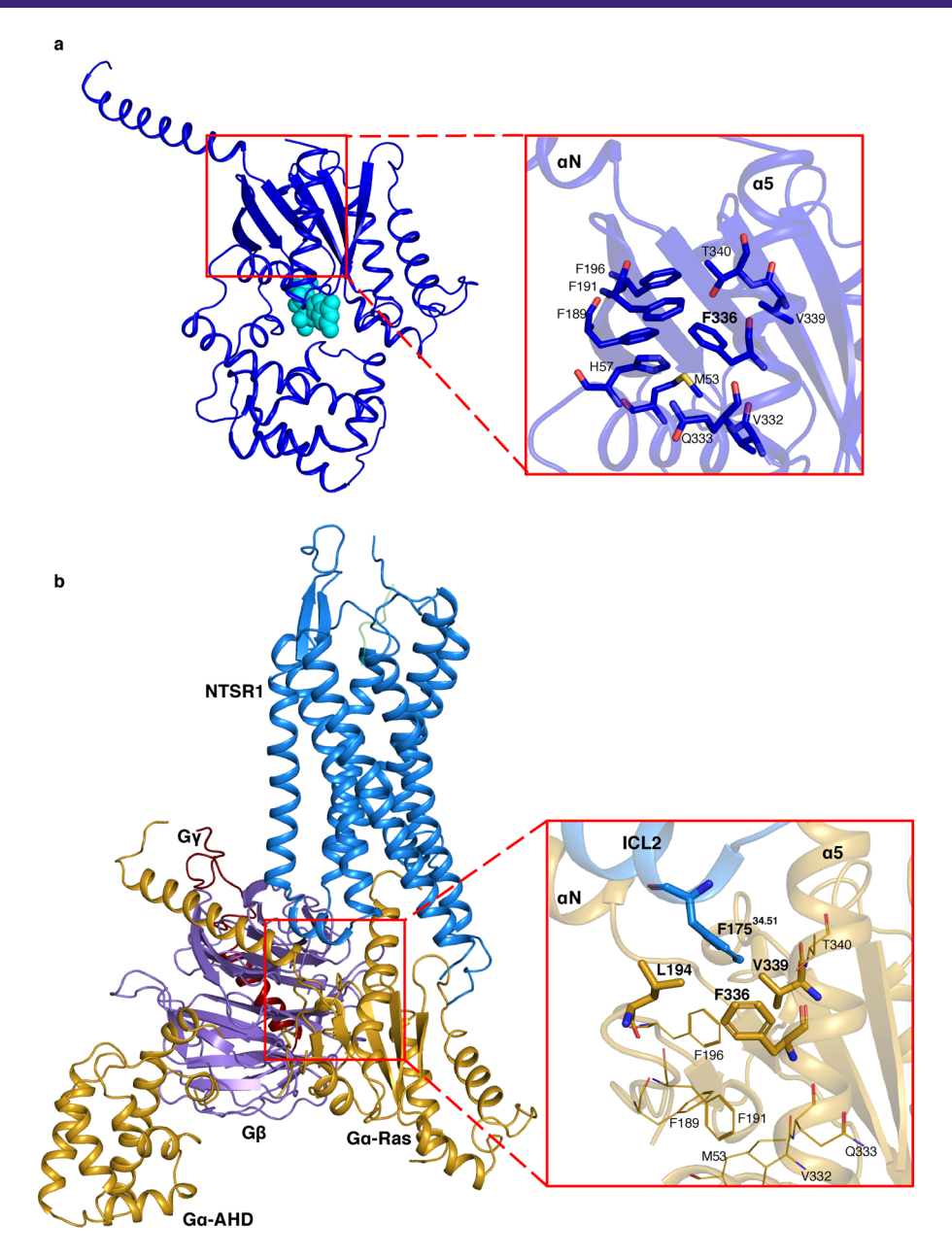
Extended Data Fig. 5 | Structure and position of the α-helical domain (AHD). a, Density maps and models showing the interaction between $G\beta_1$ (purple) and $G\alpha_1$ AHD (gold) in the canonical state. Zoom-in view of the $G\alpha_1$ AHD is shown. **b**, Density maps and models showing the interaction between $G\beta_1$ (purple) and $G\alpha_1$ AHD (dark green) in the noncanonical state. Zoom-in view of the $G\alpha_1$ AHD is shown. The models in (**a**) and (**b**) are superposed on the $G\beta_1$ subunits and are shown in the same view. AHD in both states interacts with the second and third blades of $G\beta_1$. **c-f**, Comparison of the AHD of the canonical state NTS-NTSR1-Gi-cND (gold) with **c**, A crystal structure of GDP- G_1 (blue; PDB 1GP2), **d**, A crystal structure of β_2 AR- G_s with nanobody Nb35 (AHD is dark red and Nb35 is green; PDB 3SN6), **e**, A cryo-EM structure of Rhodopsin- G_1 with Fab G50 (AHD is pink and Fab G50 is green; PDB 6CMO), and **f**, A cryo-EM structure of Smoothened- G_1 with Fab G50 (AHD is light blue and Fab G50 is green; PDB 6OTO). The models are superposed on the Gα Ras-like domain.



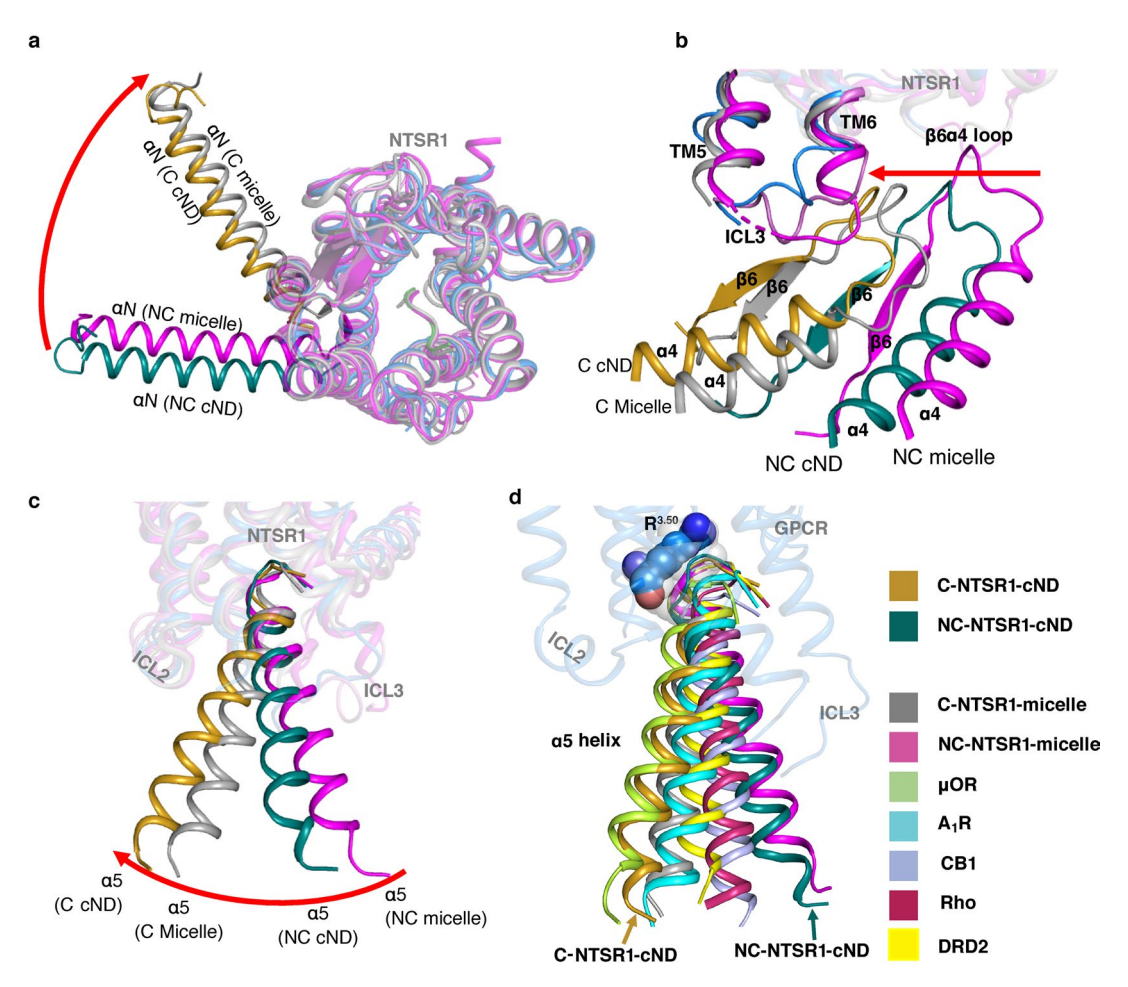
Extended Data Fig. 6 | Cryo-EM structure of the NTS-NTSR1-G_i complex in lipid nanodiscs and the interaction with lipid. a, Three views of the cryo-EM density map of the NTS-NTSR1-G_i-cND complex in the canonical state. **b**, Three views of the cryo-EM density map of the NTS-NTSR1-G_i-cND complex in the noncanonical state. The maps in panels (a) and (b) are low-pass filtered to 5 Å and colored by subunit. **c**, Two views of NTS-NTSR1 surrounded by nanodisc density. The transmembrane helices are shown in cylinder representation using the rainbow coloring scheme. ICL2 and helix H8 are partially submerged in lipid.



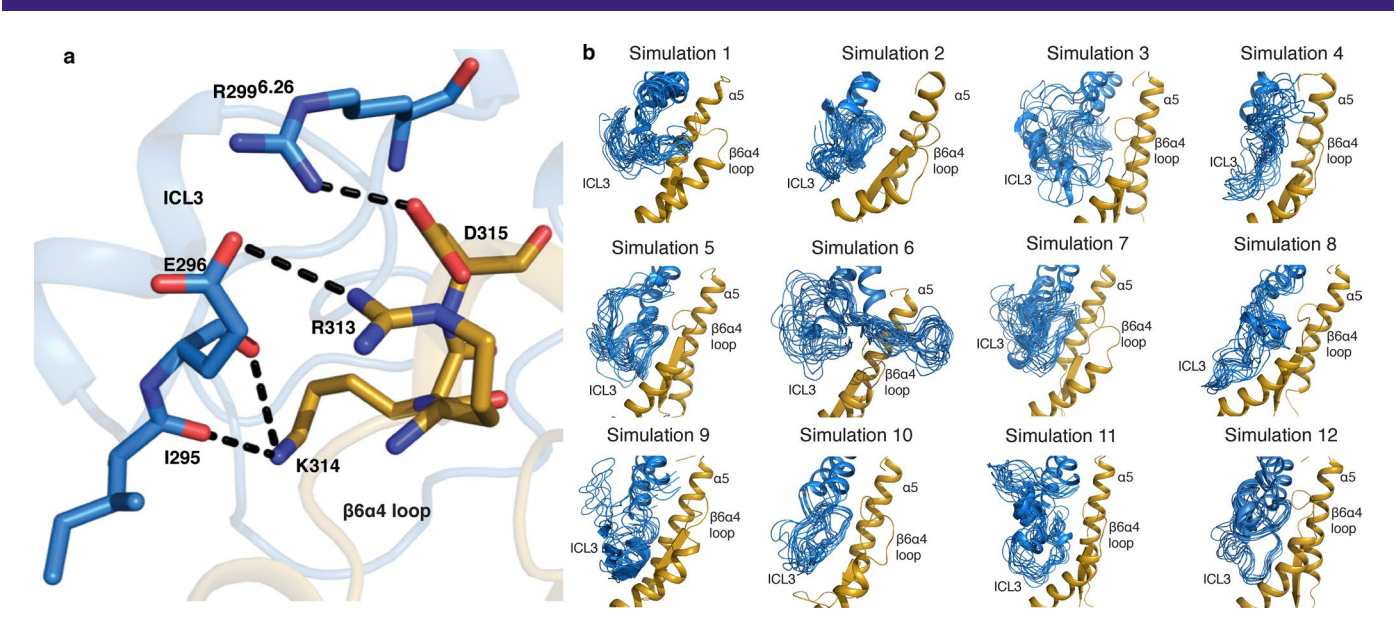
Extended Data Fig. 7 | Impact of the lipid bilayer on the structure of NTSR1. a, Comparison between the cryo-EM structures of the canonical states of NTSR1 (with G_i) in lipid bilayer (blue) and detergent (gray, PDB 6OS9). TM6 is shifted by 1.6 Å (based on $C\alpha$ of V309) inwards in lipid bilayer. Right, comparison of the C-NTS-NTSR1-Gi-cND model (blue) with the density map of C-NTSR1-Gi-micelle (pink) (EMD-20180, low-pass filtered to 5 Å) confirms this shift to be significant. **b**, Structural comparison between the crystal structure of NTSR1 in detergent (green, PDB 4XEE) and the cryo-EM structure of the canonical state of NTSR1 in complex with G_i in detergent (gray, PDB 6OS9). The atomic models in (a) and (b) are superposed on NTSR1. **c**, Comparison of the localization of TM5-TM6 relative to α 5-helix of $G\alpha$ in class A GPCR- G_i complex structures, including the canonical state NTSR1 (blue) in complex with G_i (gold) structure reported in the current study, μ 0R- G_i (lime green; PDB 6DDE), Rho- G_i (hot pink; PDB 6CMO), A_i R- G_i (cyan; PDB 6D9H), and CB1- G_i (purple; PDB 6N4B). The models are superposed on the Ras-like domain of $G\alpha$.



Extended Data Fig. 8 | ICL2 interaction with a hydrophobic pocket of G_i . a, Structure of GDP- $G\alpha_i$ showing a hydrophobic network surrounding F336 in the zoomed-in view. Residues involved in the network are shown as sticks. b, Atomic model of C-NTS-NTSR1- G_i -cND showing insertion of F175^{34.51} from ICL2 of NTSR1 into a hydrophobic pocket involving residues F336, L194 and V339 of $G\alpha_i$. Residues involved in the network are shown as sticks. Residues from the network in (a) are shown in lines. A transition of F336 on $G\alpha_i$ from the network in (a) in the GDP-bound state to a new network in (b) in the NTSR1-bound state is observed.



Extended Data Fig. 9 | Comparison of NTSR1-G_i interaction in lipid bilayer with detergent micelles. a-c, Superposed structure of C-state NTSR1 (blue) and G α (gold) in cND, NC-state NTSR1 (orchid) and G α (dark cyan) in cND, C-state NTSR1 and G α in micelle (gray, PDB 6OS9), NC-state NTSR1 and G α in micelle (magenta, 6OSA). The models are superposed on NTSR1. **a**, extracellular view of NTSR1 and α N-helix; **b**, side view of NTSR1 ICL3 and α 4 β 6 loop; **c**, side view of NTSR1 and α 5-helix. **d**, Comparison of the localization of α 5-helix relative to GPCR in class A GPCR-G_i complex structures, including the canonical (gold) state and noncanonical (dark cyan) state structure reported in the current study, canonical (gray) and noncanonical (magenta) state of NTSR1-G_i in detergent micelle, μ 0R-G_i (lime green; PDB 6DDE), A₁R-G_i (cyan; PDB 6D9H), CB1-G_i (purple; PDB 6N4B), Rho-G_i (hot pink; PDB 6CMO) and DRD2-G_i (yellow; PDB 6VMS). The structures are superposed on the GPCR. Residue R^{3.50} is shown as colored spheres in C-state NTSR1 and as partially transparent gray spheres in the other GPCRs.



Extended Data Fig. 10 | Molecular dynamics (MD) simulation for the interaction between ICL3 and the \alpha4\beta6 loop. a, MD simulation showing the salt bridges and hydrogen bonds that form between TM6-ICL3 and α 4 β 6 loop in the canonical state of NTS-NTSR1-Gi-cND represented by simulation 12. **b**, Dynamics of ICL3 for each independent simulation of the canonical state of NTS-NTSR1-G_i-cND. Frames are sampled every 40 ns from each individual simulation. All 12 simulations show various interactions including salt bridges/hydrogen bonds between ICL3 and the α 4 β 6 loop. An example of detailed interactions is shown in (**a**). NTSR1 is colored in blue and G_i in gold in (**a,b**).

nature research

Gerhard Wagner Mahmoud L. Nasr

Corresponding author(s): Alan Brown

Last updated by author(s): Dec 13, 2020

Reporting Summary

Nature Research wishes to improve the reproducibility of the work that we publish. This form provides structure for consistency and transparency in reporting. For further information on Nature Research policies, see our Editorial Policies and the Editorial Policy Checklist.

<u> </u>					
Si	1	+1	c	H١.	\sim
. 11	_		, n		

For	all statistical analyses, confirm that the following items are present in the figure legend, table legend, main text, or Methods section.
n/a	Confirmed
	The exact sample size (n) for each experimental group/condition, given as a discrete number and unit of measurement
	A statement on whether measurements were taken from distinct samples or whether the same sample was measured repeatedly
\boxtimes	The statistical test(s) used AND whether they are one- or two-sided Only common tests should be described solely by name; describe more complex techniques in the Methods section.
X	A description of all covariates tested
X	A description of any assumptions or corrections, such as tests of normality and adjustment for multiple comparisons
\boxtimes	A full description of the statistical parameters including central tendency (e.g. means) or other basic estimates (e.g. regression coefficient AND variation (e.g. standard deviation) or associated estimates of uncertainty (e.g. confidence intervals)
\boxtimes	For null hypothesis testing, the test statistic (e.g. <i>F</i> , <i>t</i> , <i>r</i>) with confidence intervals, effect sizes, degrees of freedom and <i>P</i> value noted <i>Give P values as exact values whenever suitable.</i>
\boxtimes	For Bayesian analysis, information on the choice of priors and Markov chain Monte Carlo settings
\boxtimes	For hierarchical and complex designs, identification of the appropriate level for tests and full reporting of outcomes
\times	Estimates of effect sizes (e.g. Cohen's <i>d</i> , Pearson's <i>r</i>), indicating how they were calculated
	Our web collection on <u>statistics for biologists</u> contains articles on many of the points above.

Software and code

Policy information about <u>availability of computer code</u>

Data collection

Automated data collection on the Titan Krios was performed using serialEM (verision 3.6).

Data analysis

The following software was used in this study: Graphpad Prism 8.4.1, Spectrum Manager 2, MO Affinity Analysis 3, ForteBio 11.0, NMRPipe 10.9, Sparky 3.115, MotionCor2, CTFFIND4, EMAN v2.2, crYOLO v1.01, RELION-3.0, RELION-3.1-beta, UCSF Chimera v1.14, Pymol v2.3, Coot v0.9, MolProbity v4.3.1, Maestro, CHARMM-GUI, Amber18, Amber FF14SB, Amber Lipid17, TIP3P model, AmberTools 18, VMD 1.9.4, Phenix v1.18.2-3874

For manuscripts utilizing custom algorithms or software that are central to the research but not yet described in published literature, software must be made available to editors and reviewers. We strongly encourage code deposition in a community repository (e.g. GitHub). See the Nature Research guidelines for submitting code & software for further information.

Data

Policy information about availability of data

All manuscripts must include a data availability statement. This statement should provide the following information, where applicable:

- Accession codes, unique identifiers, or web links for publicly available datasets
- A list of figures that have associated raw data
- A description of any restrictions on data availability

EM density maps and atomic models of the NTS–NTSR1–Gi complex in lipid nanodiscs have been deposited in the Electron Microscopy Data Bank (EMDB) and wwPDB, respectively, under accession codes EMD-23099 and PDB 7LOP (canonical state without AHD), EMD-23100 and PDB 7LOQ (canonical state with AHD), EMD-23101 and PDB 7LOR (noncanonical state without AHD), and EMD-23102 and PDB 7LOS (noncanonical state with AHD).

Fi	اما		-0	ne	cif	ic	re	n	∩ r	÷i	n	σ
		U	1-2	νc	CH	IC	IC	יץ	JI	U	11	8

Field-spe	ecific re	porting				
Please select the or	ne below that is	s the best fit for your research. If you are not sure, read the appropriate sections before making your selection.				
Life sciences Behavioural & social sciences Ecological, evolutionary & environmental sciences						
For a reference copy of t	the document with	all sections, see <u>nature.com/documents/nr-reporting-summary-flat.pdf</u>				
Life scier	nces stu	udy design				
All studies must dis	close on these	points even when the disclosure is negative.				
Sample size	IP1 production functional assays were performed as 4 biologically independent experiments in duplicate. For BLI experiments, three independent biological samples were used for the measurement of NTSR1-Gi binding in cNDs; two independent biological samples were used for the measurement of GTPrS dissociation and empty cND-Gi binding. For MST experiments, two independent biological samples were used for the measurement in POPC/POPG (3/2) cND, detergent micelles, POPC cND, POPG cND and the Alanine mutant TM86V-L167R (E66A/K176A/K178A/S182A/R185A) in POPC/POPG (3/2) cND, each with three technical repeats; one biological sample was used for the measurement in POPC/POPG/CHS (3/2/0.3) cND with three technical repeats; two biological samples were used for measurement in empty POPC/POPG (3/2) cND. For cryo-EM studies, ~1.7 million single particle images were used as initial input in order to produce the 3D reconstructions in RELION-3.0 or RELION-3.1-beta. Particle numbers for different reconstructions, as described in Extended Data Fig. 3c were selected to produce the resolutions (FSC=0.143) reported in Table 1.					
Data exclusions	No data was ex	cluded from the analyses.				
Replication	All attempts at replication of functional assays succeeded. Cryo-EM analysis was performed on ~1.7 million particles picked in an automated fashion from a total of 23,677 movie stacks.					
Randomization	No randomization was attempted or needed. This was not a clinical trial or animal study that is dependent on randomization. All variables could be controlled.					
Blinding	No blinding was attempted or needed. There was no group allocation performed in this study.					
We require information system or method list Materials & exp	on from authors a ted is relevant to perimental s					
n/a Involved in the study Antibodies ChIP-seq Ch						
☐ ☐ Eukaryotic cell lines ☐ ☐ Flow cytometry						
Palaeontology and archaeology MRI-based neuroimaging						
Animals and other organisms						
Human research participants Clinical data						
Dual use research of concern						
—,—						
Eukaryotic c	ell lines					
Policy information						
Cell line source(s)	Sf9, Expression Systems, Cat 94-001S. HEK293T/17 cells, ATCC, CRL-11268				
Authentication		Cell lines are maintained by the supplier. No additional authentication was performed by the authors of this study.				
Mycoplasma con	coplasma contamination Cell lines are tested by manufacturer for contamination and no additional testing was performed by the authors of this					
Commonly miside	monly misidentified lines (N/A					